

Fault-Tolerant Belief Propagation for Practical Quantum Memory

Kao-Yueh Kuo and Ching-Yi Lai

Abstract—A fault-tolerant approach to reliable quantum memory is essential for scalable quantum computing, as physical qubits are susceptible to noise. Quantum error correction (QEC) must be continuously performed to prolong the memory lifetime. In QEC, error syndromes are generated rapidly, often within the execution time of a few quantum gates, requiring decoders to process this error data with equal speed. A typical QEC cycle involves multiple rounds of syndrome measurements, causing potential error locations to scale rapidly with the code size and the number of measurement rounds. However, no such decoders currently exist for general quantum low-density parity-check codes. In this paper, we propose a fault-tolerant belief propagation (FTBP) decoder that utilizes a space-time Tanner graph across multiple rounds of syndrome extraction with mixed-alphabet error variables. To enhance FTBP, we introduce a technique of probabilistic error consolidation to mitigate degeneracy effects and short cycles. Additionally, we propose an adaptive sliding window procedure that captures long error events across window boundaries and adjusts the decoding in real time. Our simulations demonstrate high error thresholds of 0.4%–0.87% and strong error-floor performance for topological code families, including rotated toric, toric color, and twisted XZZX toric codes.

I. INTRODUCTION

In the pursuit of scalable quantum computing, protecting quantum information through quantum error correction (QEC) is crucial, as quantum systems are inherently vulnerable to noise [1]–[5]. To achieve fault-tolerant quantum computation (FTQC) [6]–[9], it is essential to develop reliable quantum memory that supports the long-term storage of quantum information. Among various QEC schemes, topological codes, such as surface codes [10] and color codes [11], [12], have emerged as leading candidates due to their advantageous properties, including local stabilizer measurements and high thresholds for fault tolerance [13]–[16]. On the other hand, quantum low-density parity-check (QLDPC) codes offer a distinct advantage by providing higher code rates and reduced overhead for quantum memory, assuming higher qubit connectivity [17]–[22]. Additionally, QLDPC codes may also exhibit high thresholds for fault tolerance [23], making them a promising alternative in FTQC.

In reality, every component in a quantum circuit is potentially faulty, and errors can propagate throughout the system. This presents a challenge for fault-tolerant error correction (FTEC) when using imperfect components. In QEC, error syndromes are generated rapidly, often within the execution time of a few quantum gates, especially for QLDPC codes with low-weight checks. To ensure reliable quantum memory, active QEC must be implemented quickly enough to prevent logical errors due to error accumulation. Specifically, the rate at which error syndrome bits are processed should match or exceed their

generation rate [24]. When quantum memory is protected by a quantum code with a minimum distance d , a typical QEC cycle involves $O(d)$ rounds of syndrome measurements [13], resulting in $O(d^3)$ potential error locations for a code of length $O(d^2)$.

Traditional decoders like minimum-weight perfect matching (MWPM) [13], [14], [25], [26], union-find (UF) [27], [28], and belief propagation (BP) [17], [29]–[35] combined with ordered statistic decoding (OSD) [21], [36], [37] are commonly used for FTEC. MWPM is effective for surface and toric codes but has computational complexity cubic in the number of error variables. UF offers nearly linear complexity, making it more efficient, but it has suboptimal performance. Both MWPM and UF are limited to specific topological codes. BP-OSD, however, is a more general decoder for QLDPC codes [23], combining BP for error likelihood estimation with OSD for better correction. While BP-OSD improves performance, it also incurs at least cubic complexity, making it computationally intensive (i.e. $O(d^9)$ for a code of distance d). Since large-distance quantum codes are essential for large-scale quantum systems, a decoder with complexity nearly linear in the number of error variables is highly desirable. This becomes particularly crucial when we aim to develop an error-correction scheme to enhance the lifetime of quantum memory.

In this paper, we propose a BP-based solution for FTEC. BP has been adapted to decode quantum codes in the code capacity model with perfect error syndromes [17], [33]–[35], [38]–[40], quantum data-syndrome codes [41], [42], and the phenomenological noise model [42]. We introduce a fault-tolerant belief propagation (FTBP) decoding algorithm for general QLDPC codes, covering both CSS codes [2], [3] and non-CSS codes, under the circuit-level noise model. Our approach consists of several key components for achieving fault-tolerant quantum memory, which will be explained as follows.

A quantum stabilizer code can be viewed as an additive quaternary code generated by a binary matrix [43]. In the circuit-level noise model, single-qubit errors are common, while a two-qubit gate can experience 16 types of errors, and qubit measurement errors are binary, making this analogous to an additive code over a mixed alphabet consisting of binary, quaternary, and 16-ary symbols. By introducing a mixed-alphabet error syndrome representation, we construct a generalized check matrix for a syndrome extraction circuit over multiple rounds. This generalized check matrix defines the linear relationship between the actual errors and the observed binary error syndromes. Consequently, we propose

an FTBP decoding algorithm to handle this mixed-alphabet decoding problem, where all transmitted messages are scalars, extending our previous decoders in [34], [35]. For reference, the FTEC decoding problem also induces a binary version of syndrome and check matrix relations for decoding X and Z errors [44], [45]. However, correlations between single- and two-qubit Pauli errors may be overlooked, potentially resulting in suboptimal solutions.

By applying appropriate row operations on the generalized check matrix and transforming the observed syndrome, we can derive a sparse matrix in the form of a lower block bidiagonal Toeplitz matrix, ensuring that any localized error affects only two rounds of error syndromes. This structure facilitates the construction of a space-time Tanner graph over multiple rounds of syndrome extraction, capturing the evolution of errors over time. By incorporating both spatial and temporal correlations, this sparse graph representation allows for more effective error correction. This suggests that the complexity of FTBP for a d^2 -qubit code with distance d , $O(1)$ stabilizer weights and a decoding window of $O(d)$ rounds of syndrome extraction is $O(d^3 \log d)$.

However, the presence of multiple two-qubit gates introduces significantly more degenerate errors in the decoding problem, resulting in numerous short cycles, which are known to cause failures in BP decoding. A direct application of FTBP on the generalized check matrix with the usual error distribution initialization leads to poor decoding performance (see Fig. 9). To mitigate these degeneracy effects, we propose a technique called probabilistic error consolidation. Probabilistic error consolidation reduces the problem size by adjusting the probabilities of degenerate errors that correspond to the same syndrome and have the same residue errors on the data qubits, consolidating them into a single representative error while eliminating the others. This process decouples higher-order error variables into lower-order ones for probabilistic consolidation. This not only simplifies the decoding process but also helps reduce the number of short cycles in the Tanner graph.

Finally, for practical memory lifetime decoding, sliding window decoding is necessary to maintain reasonable decoding complexity [13], [46]–[48]. In this approach, the decoder processes a fixed number of syndrome extraction rounds before advancing by a specified number of rounds, known as the window offset. We observe that long error events across window boundaries typically degrade the performance of window decoding with a fixed window offset. To enhance the lifetime of quantum memory, we introduce a simple adaptive sliding window decoding procedure. By identifying potential boundary-crossing events, we can dynamically adjust the window offset, ensuring that the decoding process remains both effective and efficient. This windowed approach also enables real-time error correction, making it well-suited for practical implementations.

Together, these techniques form a comprehensive framework for FTBP, offering a scalable and efficient solution for reliable quantum memory in practical quantum computing systems. To validate our approach, we conduct memory lifetime simulations on the $[[d^2, 2, d]]$ rotated toric codes (with

even d) [10], [12], $[[\frac{9}{8}d^2, 4, d]]$ rotated 6.6.6 toric color codes (with d a multiple of 4) [11], [12], and $[[\frac{(d^2+1)}{2}, 1, d]]$ twisted XZZX toric codes (with odd d) [49]–[51]. In our experience, decoding problems induced by topological codes in the code capacity and phenomenological noise models tend to be more difficult compared to those from quantum codes with nonlocal stabilizers, such as bicycle codes [35], [42], which is why we focus on topological codes under the circuit-level noise model. However, our methods are applicable to general QLDPC codes.

In our simulations, the use of adaptive sliding window decoding and probabilistic error consolidation techniques significantly enhances the FTBP decoding performance. Additionally, a window size of d to $2d$ rounds is generally sufficient for these topological codes with minimum distance d , as performance saturates beyond $2d$ rounds. Based on these techniques, the FTBP decoding threshold for rotated toric codes is estimated to be 0.75% using the finite-size scaling ansatz [52], [53], which is comparable to the MWPM decoding threshold for toric and surface codes [13], [14], [54], [55], estimated to be roughly 0.75%–1%. Similarly, we observe a threshold of approximately 0.4%–0.59% for the rotated 6.6.6 color codes, which surpasses previous thresholds for color-type codes using modified MWPM algorithms. Furthermore, we provide the first threshold estimation of around 0.75%–0.87% for the twisted XZZX toric codes.

On the other hand, FTBP also exhibits good error floor performance for these topological codes. Notably, the rotated color codes have a lower error floor than the rotated toric codes, highlighting the effectiveness of color codes for low error rate performance, which is crucial for applications in quantum computing.

By utilizing adaptive sliding windows and probabilistic error consolidation techniques, FTBP significantly reduces the overhead associated with decoding while maintaining high performance. Its nearly-linear scaling makes it particularly suited for practical quantum memory applications. Moreover, it is applicable to general QLDPC codes, paving the way for the construction of improved quantum codes.

The paper is organized as follows. In Sec. II, we introduce quantum stabilizer codes and the circuit-level noise model. In Sec. III, we construct a generalized check matrix for a syndrome extraction circuit, define the circuit-level decoding problem, and propose the FTBP decoding algorithm. We then derive a sparse generalized check matrix that induces a space-time Tanner graph in Sec. IV. Additionally, we discuss several problem reduction techniques, including error merging and probabilistic error consolidation. In Sec. V, we discuss the lifetime of quantum memory and propose an adaptive sliding window decoding approach. Finally, we conduct several simulations in Sec. VI to demonstrate the effectiveness of these techniques, followed by our conclusion.

II. QUANTUM STABILIZER CODES

The Pauli matrices are $I = \begin{bmatrix} 1 & 0 \\ 0 & 1 \end{bmatrix}$, $X = \begin{bmatrix} 0 & 1 \\ 1 & 0 \end{bmatrix}$, $Y = \begin{bmatrix} 0 & -i \\ i & 0 \end{bmatrix}$, and $Z = \begin{bmatrix} 1 & 0 \\ 0 & -1 \end{bmatrix}$. For convenience, an n -fold Pauli operator $E = cE_1 \otimes \cdots \otimes E_n$ for $c \in \{\pm 1, \pm i\}$ and

$E_j \in \{I, X, Y, Z\}$ may occasionally be represented as a row vector $E = (E_1, \dots, E_n) \in \{I, X, Y, Z\}^{1 \times n}$, since the phase does not impact our examination of Pauli error decoding problems. An identity operator $I^{\otimes n}$ for any n will be simply denoted by I . The weight of E , denoted $\text{wt}(E)$, is the number of its nonidentity Pauli components. We use X_j or Z_j to represent a nontrivial Pauli matrix applied to qubit j , while operating trivially on the other qubits. For $u = (u_1, \dots, u_n), v = (v_1, \dots, v_n) \in \{0, 1\}^n$, we define

$$Z^u X^v = \prod_{i=1}^n Z_i^{u_i} \prod_{j=1}^n X_j^{v_j} = (Z_1^{u_1} X_1^{v_1}, \dots, Z_n^{u_n} X_n^{v_n}). \quad (1)$$

For example, $X \otimes I \otimes Z = (X, I, Z) = X_1 Z_3$. In addition, an n -fold Pauli operator $Z^u X^v$ can be represented by a binary string $(u, v) \in \{0, 1\}^{2n}$ when the global phase is not important.

Any two Pauli operators either commute or anticommute. Thus, we define a bilinear form $*$ on two Pauli operators E and F by

$$E * F = \begin{cases} 0, & \text{if } E \text{ and } F \text{ commute;} \\ 1, & \text{if } E \text{ and } F \text{ anticommute.} \end{cases} \quad (2)$$

A. Code capacity model

Let \mathcal{S} be an abelian group of n -fold Pauli operators such that $-I \notin \mathcal{S}$. The joint $(+1)$ -eigenspace of \mathcal{S} is called a stabilizer code, which includes n -qubit states that are fixed by \mathcal{S} . Suppose that \mathcal{S} is generated by $n - k$ independent generators; then the code is denoted as an $[[n, k]]$ stabilizer code. The group \mathcal{S} is called the stabilizer group, and its elements are called stabilizers for the code.

A Pauli error E occurring on a state in the codespace can be detected if it anticommutes with any of its stabilizers. Assume that $m \geq n - k$ stabilizers $g_1, g_2, \dots, g_m \in \{I, X, Y, Z\}^n$ are perfectly measured with binary outcomes $s = (s_1, \dots, s_m) \in \{0, 1\}^m$, where

$$s_i = E * g_i. \quad (3)$$

The binary vector s is called the error syndrome of E . If a Pauli error is a stabilizer, it does not affect the codespace. A stabilizer code has minimum distance d if the weight of any non-stabilizer, undetectable Pauli error is at least d . Such a code is referred to as an $[[n, k, d]]$ stabilizer code.

If two Pauli errors have the same effect on the codespace and cannot be distinguished by the measured error syndrome, they are referred to as *degenerate* errors. This degeneracy must be taken into account when addressing the decoding problem for a stabilizer code.

Figure 1 illustrates the raw syndrome extraction process for stabilizers of weight 4. When only Pauli errors are considered and syndrome measurements are assumed to be perfect, this is referred to as the *code capacity model*, which is used to assess the theoretical limits of quantum error-correcting codes.

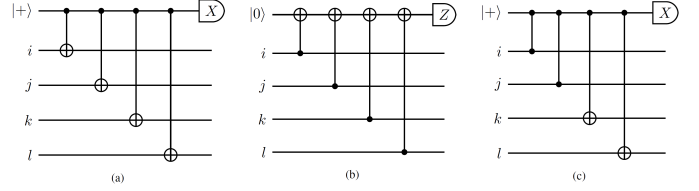


Fig. 1. Measurement circuits for (a) $X_i X_j X_k X_l$, (b) $Z_i Z_j Z_k Z_l$, and (c) $X_i Z_j Z_k X_l$, applied to the corresponding data qubits i, j, k , and l in sequence.

B. Circuit-level noise model

In the circuit-level noise model [13], [14], each location in a quantum circuit, including quantum gates, measurements, state preparation, and idle qubits, is susceptible to faults. Additionally, errors can propagate through controlled-phase (CZ) and controlled-NOT (CNOT) gates within the quantum circuit. As a result, fault-tolerant syndrome extraction procedures are crucial to obtaining reliable measurement outcomes that can effectively prevent error accumulation [56].

For topological codes with low-weight stabilizer generators, repeatedly applying the raw syndrome extraction method is sufficient to achieve fault-tolerant syndrome extraction [13]. In this work, we follow this procedure for simplicity, with the understanding that it can be directly extended to general fault-tolerant quantum error correction protocols. Specifically, we focus on topological quantum codes with local, low-weight stabilizers [10], particularly those defined on a torus. These include the $[[d^2, 2, d]]$ rotated toric codes (with even d) [10], [12], $[[\frac{9}{8}d^2, 4, d]]$ rotated 6.6.6 toric color codes (with d a multiple of 4) [11], [12], and $[[\frac{(d^2+1)}{2}, 1, d]]$ twisted XZZX toric codes (with odd d) [49]–[51].

For clarity, we illustrate the code lattices in Figs. 2, 3, and 4, respectively, and define the corresponding measurement orders for the stabilizers. Figure 2(a) shows a lattice of a rotated 2×2 toric code with four stabilizers given by $\begin{bmatrix} Z & Z & Z & Z \\ X & X & X & X \\ Z & Z & Z & Z \\ X & X & X & X \end{bmatrix}$, where two of the rows are redundant. All four syndrome measurements can be performed in parallel across four depths. Based on the measurement order shown in Fig. 2(a), the syndrome extraction sequence is as follows:

	depth 1	depth 2	depth 3	depth 4
ancilla 1	Z_1	Z_4	Z_3	Z_2
ancilla 2	X_2	X_3	X_4	X_1
ancilla 3	Z_3	Z_2	Z_1	Z_4
ancilla 4	X_4	X_1	X_2	X_3

This sequence defines a round of syndrome extraction. Similar syndrome extraction circuits can be defined for the toric color codes and twisted XZZX toric codes.

III. CIRCUIT-LEVEL NOISE DECODING PROBLEM

In this section, we explore quantum memory protected by an n -qubit topological code, where quantum information is encoded in the codespace. A continuous syndrome measurement procedure is constantly applied to the encoded quantum memory, followed by error correction based on the measurement outcomes.

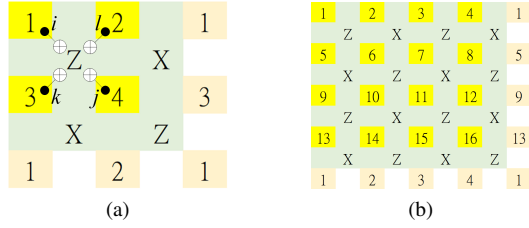


Fig. 2. The lattice representation of the family of $[[d^2, 2, d]]$ toric codes is illustrated for (a) $d = 2$ and (b) $d = 4$. Each data qubit is represented by a yellow box labeled with a number ranging from 1 to d^2 . The orange boxes on the boundary correspond to the yellow boxes with the same numbers, indicating the connectivity of qubits since the lattice wraps around a torus. Green boxes labeled with X or Z, surrounded by four data qubits labeled as (i, j, k, l) , represent stabilizers of the form $X_i X_j X_k X_l$ or $Z_i Z_j Z_k Z_l$. The order (i, j, k, l) also signifies the order in which measurements are performed. For instance, in (a), the upper-left label Z corresponds to the measurement order $(1, 4, 3, 2)$, indicating that a stabilizer $Z_1 Z_4 Z_3 Z_2$ is measured in this specific order. All stabilizers in this code family follow this measurement order. This representation visually demonstrates the structure of the toric code and the sequence in which stabilizers are measured on the lattice.

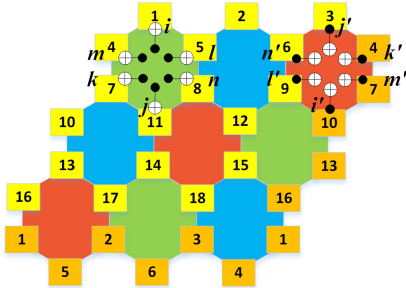


Fig. 3. The lattice of the $[[\frac{8}{3}d^2, 4, d]]$ toric color code with $d = 4$. The qubits are labeled similarly to those in Fig. 2. Every plaquette represents both an X and a Z stabilizer, each operating on the six data qubits surrounding the plaquette. For full parallelism, the X and Z stabilizers are measured in different orders. The X stabilizer follows the measurement order (i, j, k, l, m, n) as shown in a green plaquette, while the Z stabilizer follows the measurement order (i', j', k', l', m', n') as shown in a red plaquette.

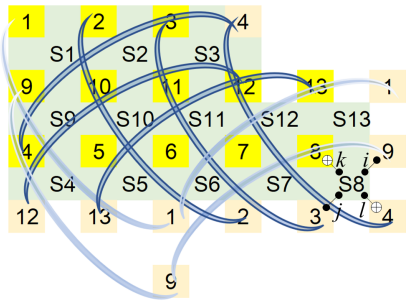


Fig. 4. The lattice of the $[[L^2 + (L-1)^2, 1, 2L-1]] = [[(d^2+1)/2, 1, d]]$ twisted XZZX toric code with $L = 3$ ($d = 5$), corresponding to a $[[13, 1, 5]]$ code. Its stabilizers are cyclicly generated by $Z_2 Z_9 X_1 X_{10}$. All the stabilizers can be measured in parallel, following a similar order. For example, stabilizer S8 is $Z_9 Z_3 X_8 X_4$, as shown in the figure. The labels are defined similarly to those in Fig. 2.

We assume a circuit-level noise model in the quantum memory [13], [14]. Each potential error source in the syndrome extraction circuit is referred to as a *location*. For ancillary state preparation, qubits are initialized in either the $|0\rangle$ or $|+\rangle$ state. Since the $|0\rangle$ state is immune to Z errors and

the $|+\rangle$ state is immune to X errors, we assume that qubits are perfectly initialized and then may subsequently experience bit-flip or phase-flip errors. During syndrome extraction, only qubit measurements in the X and Z bases are needed, and we assume that the binary measurement outcomes are subject to flip errors. Additionally, idle qubits are subject to Pauli errors due to imperfections in the quantum memory, a phenomenon known as idle qubit error. Furthermore, we assume that every gate operation, qubit initialization, and qubit measurement takes the same unit of time. Each operation is modeled as ideal, followed by its corresponding error.

A. Generalized check matrix

A syndrome extraction procedure is specified by a circuit description, which details the sequence of gates, measurements, ancillary state preparations, and the qubits involved at each circuit depth. For instance, Fig. 5 illustrates three rounds of raw syndrome extractions for the ZZ and XX stabilizers.

In the context of fault-tolerant error correction, our objective is to control errors in such a way that the remaining errors after correction can be addressed in the subsequent error correction cycle. Essentially, we only need to ensure that the residual errors can be corrected using a perfect syndrome extraction circuit.

We will define a corresponding decoding problem within the circuit-level noise model. To apply BP to this circuit-level decoding problem, the first step involves constructing a check matrix that defines the linear relationship between potential errors and their corresponding error syndromes. This extends the concept of the generalized data-syndrome check matrix from [42], [57], [58].

Let \mathfrak{M} be a syndrome extraction circuit of N locations and M syndrome bits. Each location in \mathfrak{M} is assigned an error variable \mathcal{E}_k based on its type. In this context, we have the following types of error variables:

- 1) $b_i \in \{0, 1\}$: Ancillary qubit preparation error at ancilla i , corresponding to either $\{I, X\}$ or $\{I, Z\}$.
- 2) $C_{ij} \in \{I, X, Y, Z\}^2$: CZ or CNOT gate error at ancilla i and data qubit j .
- 3) $D_i \in \{I, X, Y, Z\}$: Idle qubit error at data qubit i .
- 4) $m_i \in \{0, 1\}$: Measurement error at ancilla i .

For illustration, the error variables at each location in Fig. 5 are indicated, where the superscript ℓ represents the ℓ -th round of syndrome extraction.

Let $\mathcal{E} = (\mathcal{E}_1, \dots, \mathcal{E}_N)$ be an N -dimensional error vector over a mixed alphabet of symbols from $\{I, X, Y, Z\}$, $\{I, X, Y, Z\}^2$, and $\{0, 1\}$, with components $b_i^{(\ell)}$, $C_{ij}^{(\ell)}$, $D_i^{(\ell)}$, and $m_i^{(\ell)}$ in the syndrome extraction circuit \mathfrak{M} . Thus, \mathcal{E} can be understood as a collection of error variables.

We model the syndrome extraction circuit \mathfrak{M} as a function that takes an error vector \mathcal{E} as input and outputs M syndrome bits $s = \mathfrak{M}(\mathcal{E}) \in \{0, 1\}^{M \times 1}$. Specifically, \mathfrak{M} is a linear function characterized by a matrix \mathcal{H} , such that

$$s = \mathfrak{M}(\mathcal{E}) = \mathcal{H} \star \mathcal{E}, \quad (4)$$

where \mathcal{H} , with dimensions $M \times N$, is referred to as a *generalized check matrix*. The operator \star is a bilinear form on two

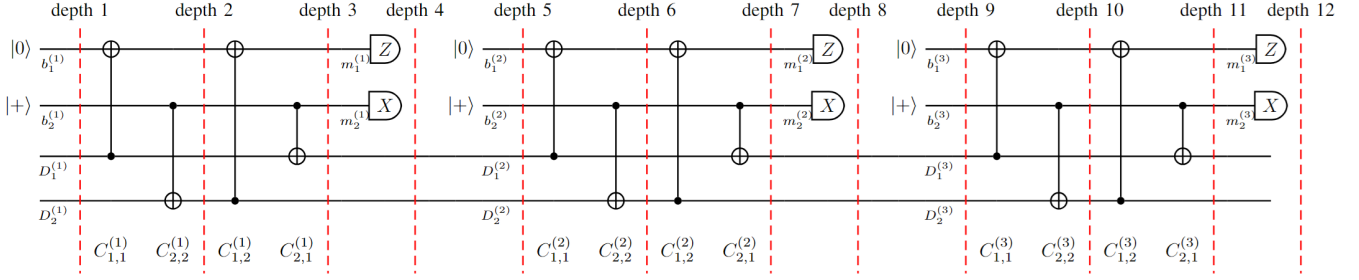


Fig. 5. Circuit for three rounds of raw syndrome extraction corresponding to the check matrix $\begin{bmatrix} Z & Z \\ X & X \end{bmatrix}$. The two stabilizers $Z_1 Z_2$ and $X_2 X_1$ are measured in two depths, with Z_1 and X_2 measured simultaneously first, followed by Z_2 and X_1 .

error vectors, $\mathcal{E} = (\mathcal{E}_1, \dots, \mathcal{E}_N)$ and $\mathcal{F} = (\mathcal{F}_1, \dots, \mathcal{F}_N)$, over a mixed alphabet of symbols from $\{I, X, Y, Z\}$, $\{I, X, Y, Z\}^2$, and $\{0, 1\}$, defined by

$$\mathcal{E} \star \mathcal{F} = \sum_{k: \mathcal{E}_k = D_i \text{ or } C_{ij}} \mathcal{E}_k \star \mathcal{F}_k + \sum_{k: \mathcal{E}_k = b_i \text{ or } m_i} \mathcal{E}_k \cdot \mathcal{F}_k \pmod{2}. \quad (5)$$

This bilinear form extends the commutation bilinear form defined in Eq. (2). We say that \mathcal{E} and \mathcal{F} are *orthogonal* if $\mathcal{E} \star \mathcal{F} = 0$. For example, two Pauli operators are orthogonal if they commute. Equation (4) extends the error syndrome calculation for stabilizer codes in the code capacity model (3).

For simplicity, we will explicitly specify only the nontrivial error components in \mathcal{E} . For instance, if $\mathcal{E}_k = m_i$, then $\mathcal{E} = \{\mathcal{E}_k = 1\}$ indicates that a measurement error occurs at location k , while all the other locations remain error-free.

Proposition 1. The generalized check matrix \mathcal{H} can be derived as follows.

- 1) If location k corresponds to an ancillary preparation error b_i or a measurement error m_i , then the k -th column of \mathcal{H} is in $\{0, 1\}^M$ and is set to be $\mathfrak{M}(\{\mathcal{E}_k = 1\})$.
- 2) If location k corresponds to an idle qubit error D_i , then the k -th column of \mathcal{H} is in $\{I, X, Y, Z\}^M$, as it must account for both X and Z syndrome measurements. Therefore, it is set to $Z^u X^v \in \{I, X, Y, Z\}^M$, where $u = \mathfrak{M}(\{\mathcal{E}_k = X\})$ and $v = \mathfrak{M}(\{\mathcal{E}_k = Z\})$.
- 3) If location k represents a CZ or CNOT gate error C_{ij} , there are 16 potential two-qubit Pauli errors and the k -th column of \mathcal{H} is in $\{I, X, Y, Z\}^{M \times 2}$. Consequently, we have to establish the syndromes of the error bases X_i, Z_i, X_j and Z_j , which are given as $u = \mathfrak{M}(\{\mathcal{E}_k = X \otimes I\})$, $v = \mathfrak{M}(\{\mathcal{E}_k = Z \otimes I\})$, $u' = \mathfrak{M}(\{\mathcal{E}_k = I \otimes X\})$, and $v' = \mathfrak{M}(\{\mathcal{E}_k = I \otimes Z\})$, respectively. Thus the k -th column of \mathcal{H} is set to

$$\begin{pmatrix} Z^{u_1} X^{v_1} & Z^{u'_1} X^{v'_1} \\ \vdots & \vdots \\ Z^{u_M} X^{v_M} & Z^{u'_M} X^{v'_M} \end{pmatrix},$$

which should be interpreted as a vector of length M over $\{I, X, Y, Z\}^2$.

Following the procedure outlined above, we can construct a generalized check matrix so that Eq. (4) holds. Note that an entry corresponding to a two-qubit Pauli error can be interpreted as two correlated single-qubit Pauli errors. Thus this generalized check matrix further extends the concept of quantum data-syndrome codes [42], [58]. For illustration, the syndrome extraction circuit for the check matrix $\begin{bmatrix} Z & Z \\ X & X \end{bmatrix}$ depicted in Fig. 5 corresponds to the generalized check matrix \mathcal{H} shown as Matrix (a) in Fig. 6.

Let $\mathcal{R}(\mathfrak{M}, \mathcal{E}) \in \{I, X, Y, Z\}^n$ denote the residual Pauli error on the data qubits of the n -qubit code after the execution of circuit \mathfrak{M} . This error can be determined by tracing the evolution of \mathcal{E} within \mathfrak{M} .

Definition 2. (Circuit-level decoding problem) Given a syndrome extraction circuit \mathfrak{M} for an n -qubit stabilizer code defined by a stabilizer group \mathcal{S} and M syndrome bits $s = \mathfrak{M}(\mathcal{E}) \in \{0, 1\}^M$ for a set of errors \mathcal{E} , output an estimate of the error set $\hat{\mathcal{E}}$ such that $\mathfrak{M}(\hat{\mathcal{E}}) = s$ and the residual error $\mathcal{R}(\mathfrak{M}, \hat{\mathcal{E}}) \mathcal{R}(\mathfrak{M}, \mathcal{E})$ can be corrected by a perfect quantum error correction procedure. \square

In the code capacity model, two Pauli errors are considered degenerate if they have the same effect on the codespace and cannot be distinguished by the measured error syndrome. This concept can be extended to the circuit-level noise model as follows.

Definition 3. Two errors \mathcal{E} and \mathcal{F} are said to be *degenerate* with respect to a syndrome extraction circuit \mathfrak{M} if they produce the same error syndrome $\mathfrak{M}(\mathcal{E}) = \mathfrak{M}(\mathcal{F})$ and result in the same residual errors on the data qubits, $\mathcal{R}(\mathfrak{M}, \mathcal{E}) = \mathcal{R}(\mathfrak{M}, \mathcal{F})$, up to stabilizers. \square

B. Belief propagation decoding

The generalized check matrix \mathcal{H} and the error syndrome relation in (4) induce a Tanner graph with various types of variable nodes and check nodes which allow us to develop a BP decoding algorithm.

In general, we are given an $M \times N$ generalized check matrix \mathcal{H} and syndrome bits $s \in \{0, 1\}^M$ for decoding. Herein, we generalize the data-syndrome BP algorithms in [41], [42] and

(a)

$D_1^{(1)}$	$D_2^{(1)}$	$C_{1,1}^{(1)}$	$C_{2,2}^{(1)}$	$C_{1,2}^{(1)}$	$C_{2,1}^{(1)}$	$m_1^{(1)}$	$m_2^{(1)}$	$b_1^{(1)}$	$b_2^{(1)}$	$D_1^{(2)}$	$D_2^{(2)}$	$C_{1,1}^{(2)}$	$C_{2,2}^{(2)}$	$C_{1,2}^{(2)}$	$C_{2,1}^{(2)}$	$m_1^{(2)}$	$m_2^{(2)}$	$b_1^{(2)}$	$b_2^{(2)}$	$D_1^{(3)}$	$D_2^{(3)}$	$C_{1,1}^{(3)}$	$C_{2,2}^{(3)}$	$C_{1,2}^{(3)}$	$C_{2,1}^{(3)}$	$m_1^{(3)}$	$m_2^{(3)}$	$b_1^{(3)}$	$b_2^{(3)}$
Z	Z	ZI	IZ	ZI		1		1		Z	Z	ZI	IZ	ZI		1		1		Z	Z	ZI	IZ	ZI		1		1	
X	X	IX	XI		XI		1		1	X	X	IX	XI		XI		1		1	X	X	IX	XI		XI		1		1
Z	Z	IZ	ZZ	IZ	IZ					Z	Z	IZ	ZZ	IZ	IZ					Z	Z	IZ	ZZ	IZ	IZ				
X	X	XX	IX	IX	IX					X	X	XX	IX	IX	IX					X	X	XX	IX	IX	IX				
Z	Z	IZ	ZZ	IZ	IZ					Z	Z	IZ	ZZ	IZ	IZ					Z	Z	IZ	ZZ	IZ	IZ				
X	X	XX	IX	IX	IX					X	X	XX	IX	IX	IX					X	X	XX	IX	IX	IX				

(b)

$D_1^{(1)}$	$D_2^{(1)}$	$C_{1,1}^{(1)}$	$C_{2,2}^{(1)}$	$C_{1,2}^{(1)}$	$C_{2,1}^{(1)}$	$m_1^{(1)}$	$m_2^{(1)}$	$b_1^{(1)}$	$b_2^{(1)}$	$D_1^{(2)}$	$D_2^{(2)}$	$C_{1,1}^{(2)}$	$C_{2,2}^{(2)}$	$C_{1,2}^{(2)}$	$C_{2,1}^{(2)}$	$m_1^{(2)}$	$m_2^{(2)}$	$b_1^{(2)}$	$b_2^{(2)}$	$D_1^{(3)}$	$D_2^{(3)}$	$C_{1,1}^{(3)}$	$C_{2,2}^{(3)}$	$C_{1,2}^{(3)}$	$C_{2,1}^{(3)}$	$m_1^{(3)}$	$m_2^{(3)}$	$b_1^{(3)}$	$b_2^{(3)}$
Z	Z	ZI	IZ	ZI		1		1		Z	Z	ZI	IZ	ZI		1		1		Z	Z	ZI	IZ	ZI		1		1	
X	X	IX	XI		XI		1		1	X	X	IX	XI		XI		1		1	X	X	IX	XI		XI		1		1
		ZZ	ZI	ZZ	IZ	1		1				ZZ	ZI	ZZ	IZ	1		1		Z	Z	ZI	IZ	ZI		1		1	
		XI	XX	IX	XX		1	1				XI	XX	IX	XX		1	1		X	X	IX	XI		XI		1		1

(c)

$D_1^{(1)}$	$C_{1,1}^{(1)}$	$C_{2,2}^{(1)}$	$C_{1,2}^{(1)}$	$C_{2,1}^{(1)}$	$m_1^{(1)}$	$m_2^{(1)}$	$D_1^{(2)}$	$C_{1,1}^{(2)}$	$C_{2,2}^{(2)}$	$C_{1,2}^{(2)}$	$C_{2,1}^{(2)}$	$m_1^{(2)}$	$m_2^{(2)}$	$D_1^{(3)}$	$C_{1,1}^{(3)}$	$C_{2,2}^{(3)}$	$C_{1,2}^{(3)}$	$C_{2,1}^{(3)}$	$m_1^{(3)}$	$m_2^{(3)}$
Z	ZI	IZ	ZI		1		Z	ZI	IZ	ZI		1		Z	ZI	IZ	ZI		1	
X	IX	XI		XI		1	X	IX	XI		XI		1	X	IX	XI		XI		1
	ZZ	ZI	ZZ	IZ	1			ZZ	ZI	ZZ	IZ	1			ZZ	ZI	ZZ	IZ	1	
	XI	XX	IX	XX		1		XI	XX	IX	XX		1		XI	XX	IX	XX		1

Fig. 6. Matrix (a) represents the generalized check matrix corresponding to the syndrome extraction circuit in Fig. 5 by Proposition 1. The columns are indexed by the location variables. An empty entry in the matrix represents a trivial element, either I or 0 . The last two rows of a matrix represent a round of perfect syndrome extraction, which is used for virtual decoding to verify whether the residual error corresponds to a logical error. Matrix (b) is a sparse matrix derived from Matrix (a) using the procedure outlined in Lemma 5. Matrix (c) is obtained by merging degenerate locations and deleting the corresponding columns from Matrix (b) by Lemma 6. Several examples of degenerate error consolidation are highlighted in different colors.

propose a decoding algorithm based on MBP in [35] to solve the circuit-level decoding problem.

We consider error vector $\mathcal{E} = (\mathcal{E}_1, \dots, \mathcal{E}_N)$, where \mathcal{E}_k is a variable of type $b_i, D_i, C_{i,j}$ or m_i defined over $\{I, X, Y, Z\}, \{I, X, Y, Z\}^2$, or $\{0, 1\}$, respectively. These variables are generated according to the following distributions.

- 1) Each single-qubit Pauli variable D_j is independently generated with depolarizing rate $\epsilon \in [0, 3/4]$, following the distribution $(p_j^I, p_j^X, p_j^Y, p_j^Z) = (1 - \epsilon, \epsilon/3, \epsilon/3, \epsilon/3)$.
- 2) Each two-qubit Pauli variable C_{ij} is independently generated with depolarizing rate $\epsilon \in [0, 3/4]$ so that $C_{ij} = I$ with probability $1 - \epsilon$ and C_{ij} is a non-identity two-qubit Pauli with probability $\epsilon/15$.
- 3) Each syndrome bit error m_j or ancillary preparation error b_j is an independent bit-flip or phase-flip error with rate $\epsilon_b \in [0, 1/2]$, following the probability distribution $(q_j^{(0)}, q_j^{(1)}) = (1 - \epsilon_b, \epsilon_b)$.

Consequently, we have initial log-likelihood ratio (LLR) vectors $\Lambda_1, \dots, \Lambda_N$ for each variable as follows.

- 1) If \mathcal{E}_k is syndrome bit error or ancillary preparation error, then Λ_k is a scalar given by

$$\Lambda_k = \ln \frac{1 - \epsilon_b}{\epsilon_b}. \quad (6)$$

- 2) If \mathcal{E}_k is a single-qubit Pauli variable D_j , then $\Lambda_k = (\Lambda_k^X, \Lambda_k^Y, \Lambda_k^Z) \in \mathbb{R}^3$, where

$$\Lambda_k^W = \ln \frac{3(1 - \epsilon)}{\epsilon} \text{ for } W \in \{X, Y, Z\}. \quad (7)$$

- 3) If \mathcal{E}_k is a two-qubit Pauli variable C_{ij} , then $\Lambda_k = (\Lambda_k^{XI}, \Lambda_k^{YI}, \Lambda_k^{ZI}, \dots, \Lambda_k^{XZ}, \Lambda_k^{YZ}, \Lambda_k^{ZZ}) \in \mathbb{R}^{15}$, where

$$\Lambda_k^W = \ln \frac{15(1 - \epsilon)}{\epsilon} \text{ for } W \in \{I, X, Y, Z\}^2 \setminus \{I\}. \quad (8)$$

The Tanner graph consists of N variable nodes corresponding to $\mathcal{E}_1, \dots, \mathcal{E}_N$ and M check nodes corresponding to the rows of \mathcal{H} . Define the set of neighboring nodes for a check node i by $\mathcal{N}(i) = \{j : \mathcal{H}_{ij} \neq I \text{ or } \mathcal{H}_{ij} \neq 0\}$, and similarly for a variable node j by $\mathcal{M}(j) = \{i : \mathcal{H}_{ij} \neq I \text{ or } \mathcal{H}_{ij} \neq 0\}$. BP performs iterative message passing on the Tanner graph to generate LLR vectors $\Gamma_1, \dots, \Gamma_N$ for the error estimate based on a given error syndrome. We propose our BP algorithm, called FTBP, for solving this circuit-level noise decoding problem, as detailed in Algorithm 1. The FTBP algorithm performs binary, quaternary, and 16-ary message computations, resulting in a slightly higher complexity.

At each iteration, the variable-to-check (V-to-C) messages $\Gamma_{j \rightarrow i}$ and check-to-variable (C-to-V) messages $\Delta_{i \rightarrow j}$ are computed as described in the algorithm. A hard decision on the error estimate is made at every iteration to check if the syndrome matches. If the syndrome does not match, the process may continue until the maximum of T_{\max} iterations is reached, at which point a failure is declared.

Given that the error syndromes are binary, Eq. (4) and the LLR distributions collectively determine whether \mathcal{E}_k and an entry of \mathcal{H} are more likely to be orthogonal. This likelihood can be quantified by a single LLR value. Consequently, all exchanged messages are scalars.

For the calculation of messages in Algorithm 1, a real-valued function λ_W for $W \in \{X, Y, Z\}$ is defined by

$$\lambda_W(\{\gamma^V : V \in \{X, Y, Z\}\}) = \ln \frac{1+e^{-\gamma^W}}{e^{-\gamma^X}+e^{-\gamma^Y}+e^{-\gamma^Z}-e^{-\gamma^W}} \quad (9)$$

for $\{\gamma^V : V \in \{X, Y, Z\}\} = \{\gamma^X, \gamma^Y, \gamma^Z\}$. It can also be extended for $W \in \{I, X, Y, Z\}^2 \setminus \{I\}$ by

$$\lambda_W(\{\gamma^V\}) = \ln \left(1 + \sum_{V \in \{I, X, Y, Z\}^2 \setminus \{I\}: V \star W = 0} e^{-\gamma^V} \right) - \ln \left(\sum_{V \in \{I, X, Y, Z\}^2: V \star W = 1} e^{-\gamma^V} \right) \quad (10)$$

for $\{\gamma^V\} = \{\gamma^{XI}, \gamma^{YI}, \gamma^{ZI}, \dots, \gamma^{ZZ}\}$. We will use $\{\gamma^V\}$ for both $V \in \{X, Y, Z\}$ and $V \in \{I, X, Y, Z\}^2 \setminus \{I\}$ without specifying the domain explicitly when it can be inferred from the context.

The check-node computation is performed using the operator \boxplus , defined for a set of ℓ real scalars $a_1, a_2, \dots, a_\ell \in \mathbb{R}$, as follows:

$$\boxplus_{j=1}^{\ell} a_j = 2 \tanh^{-1} \left(\prod_{j=1}^{\ell} \tanh \frac{a_j}{2} \right). \quad (11)$$

Remark 4. In case a two-qubit gate error location $C_{i,j}$ can be represented by two independent single-qubit error variables $C_{i,j}^a$ and $C_{i,j}^d$, where the superscripts a and d represent the ancilla and data qubits, respectively, the generalized check matrix can be treated as a matrix over $\{I, X, Y, Z\}$ and $\{0, 1\}$ and the decoding problem reduces to a generalized data-syndrome decoding problem [42], which can be handled by FTBP without 16-ary variables and 16-ary calculations.

IV. PROBLEM REDUCTION

In fault-tolerant error correction (FTEC), multiple error locations during the syndrome extraction process create a significant decoding challenge, as evidenced by the size of the underlying generalized check matrix. Estimating this size is crucial because it directly influences the instantaneous decoding complexity, a key factor in practical applications.

The complexity of the FTBP algorithm is generally $O(N\gamma T_{\max})$, where N represents the number of variables, γ is the average column weight of the generalized check matrix, and T_{\max} is the maximum number of iterations (c.f. [35], [40], [42]). Note that although 16-ary nodes contribute more to the complexity compared to binary or quaternary nodes, the overall impact remains manageable within the established complexity framework.

In this section, we demonstrate how the circuit-level decoding problem can be simplified using the FTBP algorithm.

A. BP complexity for the circuit-level decoding problem

Consider an n -qubit stabilizer code with m stabilizers being continuously measured. The measurement outcomes are collected over a specific duration, termed a (*decoding*) *window*, which is crucial for decoding. A smaller window size is

Algorithm 1 : FTBP

Input: An $M \times N$ generalized check matrix \mathcal{H} over a mixed alphabet of symbols from $\{I, X, Y, Z\}$, $\{I, X, Y, Z\}^2$, and $\{0, 1\}$, an error syndrome $s \in \{0, 1\}^M$, an integer $T_{\max} > 0$, a real scalar $\alpha > 0$, and initial LLRs $\Lambda_1, \dots, \Lambda_N$.

Initialization:

for $j \in \{1, 2, \dots, N\}$ **and** $i \in \mathcal{M}(j)$ **do**
if \mathcal{E}_j is a Pauli error, **then** let $\Gamma_{j \rightarrow i} = \lambda_{\mathcal{H}_{ij}}(\{\Lambda_j^V\})$.
else let $\Gamma_{j \rightarrow i} = \Lambda_j$.

Steps:

• **Horizontal Step (Update C-to-V Messages):**

for $i \in \{1, 2, \dots, M\}$ **and** $j \in \mathcal{N}(i)$ **do**
 $\Delta_{i \rightarrow j} = (-1)^{s_i} \boxplus_{j' \in \mathcal{N}(i) \setminus \{j\}} \Gamma_{j' \rightarrow i}$. (12)

• **Vertical Step (Marginal Distribution Part):**

for $j \in \{1, \dots, N\}$ **do**
if \mathcal{E}_j is a Pauli error, **then**
 $\Gamma_j^W = \Lambda_j^W + \frac{1}{\alpha} \sum_{\substack{i \in \mathcal{M}(j) \\ W \star \mathcal{H}_{ij} = 1}} \Delta_{i \rightarrow j}$, **for** $W \neq I$.
else $\Gamma_j = \Lambda_j + \frac{1}{\alpha} \sum_{i \in \mathcal{M}(j)} \Delta_{i \rightarrow j}$.

• **Hard Decision (and Update V-to-C Messages):**

if \mathcal{E}_j is a Pauli error, **then**
if $\Gamma_j^W > 0$ for all $W \neq I$, **then** $\hat{\mathcal{E}}_j \leftarrow I$.
else $\hat{\mathcal{E}}_j \leftarrow \arg \min_{W \neq I} \Gamma_j^W$.

else

if $\Gamma_j > 0$, **then** $\hat{\mathcal{E}}_j = 0$.
else $\hat{\mathcal{E}}_j = 1$.

Let $\hat{\mathcal{E}} = (\hat{\mathcal{E}}_1, \dots, \hat{\mathcal{E}}_N)$.

if $\mathcal{H} \star \hat{\mathcal{E}} = s$, **then return** “CONVERGE”;
else if the maximum number of iterations T_{\max} is reached, **then halt and return** “FAIL”;

else Update V-to-C Messages:

for $j \in \{1, 2, \dots, N\}$ **and** $i \in \mathcal{M}(j)$, **do**
if \mathcal{E}_j is a Pauli error, **then**

$$\Gamma_{j \rightarrow i}^W = \Gamma_j^W - (W \star \mathcal{H}_{ij}) \Delta_{i \rightarrow j}, \text{ for } W \neq I, \quad (13)$$

$$\Gamma_{j \rightarrow i} = \lambda_{\mathcal{H}_{ij}}(\Gamma_{j \rightarrow i}^X, \Gamma_{j \rightarrow i}^Y, \Gamma_{j \rightarrow i}^Z). \quad (14)$$

else $\Gamma_{j \rightarrow i} = \Gamma_j - \Delta_{i \rightarrow j}$.

Repeat from the horizontal step.

desirable as it reduces the size of the generalized check matrix. If each stabilizer measured has a weight w , each round of raw syndrome extraction requires mw CNOT or CZ gates, m ancilla preparations, and m measurements. If the decoding procedure is applied to every window of r rounds of syndrome extraction, then a generalized check matrix \mathcal{H} is of size $M \times N$, where $M = rm$ and $N = r(n + mw + 2m)$, with columns corresponding to quaternary, 16-ary, and binary entries.

For a topological code of minimum distance d and constant-

weight stabilizer measurements, such as toric codes ($w = 4$) and 6.6.6 toric color codes ($w = 6$), $m = n$ stabilizers are measured over a window of $r \leq 2d$ rounds of syndrome extraction, so the number of error locations is $N = O(d^3) = O(n^{1.5})$.

Typically, choosing $T_{\max} = O(\log N)$ is sufficient. Therefore, the key factor to analyze is the average column weight of the generalized check matrix. In topological codes, each data qubit is checked by a constant number of stabilizers in a round of syndrome extraction, which is beneficial. However, Pauli errors on the data qubits accumulate and trigger syndrome measurements in subsequent rounds of syndrome extraction. Consequently, the column weights of these Pauli errors depend on the window size, as shown by the columns corresponding to locations of types D_j and $C_{i,j}$ in Matrix (a) in Fig. 6.

As a result, the generalized check matrix has a high mean column weight of $O(d)$, which increases the BP decoding complexity. Additionally, the matrix is not sparse due to these high-weight columns. However, the following lemma demonstrates how these issues can be managed.

Lemma 5. The complexity of FTBP for an n -qubit quantum code with $O(1)$ stabilizer weights and a window of $O(\sqrt{n})$ rounds of syndrome extraction is $O(n^{1.5} \log n)$, achieved using a sparse generalized check matrix. Additionally, each variable node connects to at most two rounds of check nodes in the corresponding Tanner graph.

Proof. We begin by dividing the rows of the given generalized check matrix \mathcal{H} , as defined in Proposition 1, into r blocks corresponding to r rounds of syndrome extraction. Let $R_{i,j}$ denote the row operation that adds the i -th block to the j -th block. (The addition of two Pauli entries should be interpreted as their multiplication within the Pauli group.)

First, consider the data errors corresponding to $D_j^{(1)}$, which will accumulate on the data qubits. As a result, the entries in the first block corresponding to $D_j^{(1)}$ will appear in the other blocks as well. To eliminate these entries from the second to the r -th blocks, we apply the row operations $R_{1,2}, R_{1,3}, \dots, R_{1,r}$.

Next, consider the gate errors corresponding to $C_{i,j}^{(1)}$. These errors will be detected in the second to the r -th rounds of syndrome extraction. However, the entries in these blocks may differ from those in the first block, as not all gate errors are detected by the first round of syndrome measurements. Thus, we apply the row operations $R_{2,3}, R_{2,4}, \dots, R_{2,r}$ to eliminate these entries from the third to the r -th blocks, which also simultaneously eliminates the entries corresponding to $D_j^{(2)}$ in the third to the r -th blocks.

By continuing this process and applying $R_{i,j}$ for $j > i$, we ensure that the columns corresponding to $D_j^{(\ell)}$ remain nontrivial in only one block, while the columns corresponding to $C_{i,j}^{(\ell)}$ remain nontrivial in only two blocks. Since each stabilizer checks a constant number of data qubits, the weight of these columns remains constant.

Finally, the ancilla preparation errors and measurement errors do not propagate to other rounds of syndrome extraction. However, due to the row operations, their effects will be copied

to one additional block. Consequently, the column weights of $b_j^{(\ell)}$ or $m_j^{(\ell)}$ will be two.

By combining these results, we obtain a row operation R that sequentially applies $R_{1,2}, \dots, R_{1,r}, R_{2,3}, \dots, R_{2,r}, \dots, R_{r-1,r}$ (or equivalently $R_{r-1,r}, R_{r-2,r-1}, \dots, R_{3,2}, R_{1,2}$) to transform the given generalized check matrix \mathcal{H} into a sparse matrix $R(\mathcal{H})$ with constant column weights. Therefore, Eq. (4) becomes:

$$R(s) = R(\mathcal{H}) \star \mathcal{E}, \quad (15)$$

This transformation allows the FTBP algorithm to achieve a complexity of $O(N \log N) = O(d^3 \log d) = O(n^{1.5} \log n)$ using the new generalized check matrix $R(\mathcal{H})$. \square

For illustration, in Fig. 6, we apply a row operation to Matrix (a) to derive the sparse Matrix (b) using Lemma 5. Matrix (b) takes the form of a lower block bidiagonal Toeplitz matrix, with the same block repeated along each bidiagonal line. This structure allows the matrix to be constructed based on just two rounds of syndrome extraction.

In the following, we will consistently work with this generalized check matrix in the form of a lower block bidiagonal Toeplitz matrix. Additionally, the Tanner graph induced by this generalized check matrix will be referred to as a *space-time* Tanner graph. This term is used because an error location affects at most two rounds of syndromes, meaning a check node connects to variable nodes from the same round and possibly the previous round of the syndrome extraction circuit. As a result, we can deploy the variable and check nodes of the Tanner graph in a two-dimensional time-space domain.

Figure 7 illustrates the space-time Tanner graph of the example in Fig. 6 with three rounds of syndrome extraction, where each CNOT error variable is approximated by two single-qubit error variables for simplicity. The horizontal direction represents the timeline from left to right, while the vertical direction represents the space domain, with the variable nodes corresponding to a syndrome extraction round. Note that some variable nodes such as $D_2^{(\ell)}$ are omitted because they can be merged by Lemma 6, as will be explained in the following subsection.

B. Merging degenerate error locations of the same type

For practical purposes and decoding effectiveness, it is crucial to reduce the problem size. Degenerate errors, as defined in Def. 3, represent errors that do not need to be distinguished during the decoding process. By identifying certain degenerate errors in advance, we can optimize the generalized check matrix and initial error distributions.

Two error locations of the same type are considered degenerate if all the errors they produce are degenerate.

Lemma 6. If two error locations are degenerate, they can be merged into a single location, effectively reducing the matrix by one column (by setting its initial error rate to be 0).

- 1) If two binary variables with initial error rates ϵ_1 and ϵ_2 , respectively, are merged into one location, the new variable will have an error rate of $\epsilon' = \epsilon_1 + \epsilon_2 - 2\epsilon_1\epsilon_2$.

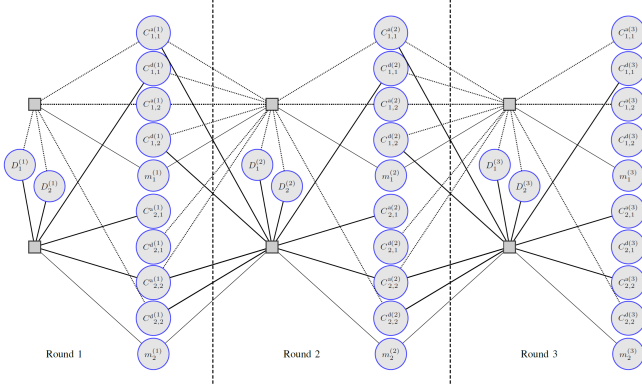


Fig. 7. The space-time Tanner graph induced from Matrix (c) in Fig. 6 uses two quaternary variables to approximate a 16-ary variable. Time progresses from left to right in the graph. The style of each edge represents its type: a thin solid line connects to a binary variable node $m_i^{(\ell)}$, a thick solid line represents an edge of type X , and a dotted line represents an edge of type Z .

- 2) If two single-qubit Pauli variables with initial error rates ϵ_1 and ϵ_2 , respectively, are merged into one location, the new variable will have an error rate of $\epsilon' = \epsilon_1 + \epsilon_2 - \frac{4}{3}\epsilon_1\epsilon_2$.
- 3) If two two-qubit Pauli variables with initial error rates ϵ_1 and ϵ_2 , respectively, are merged into one location, the new variable will have an error rate of $\epsilon' = \epsilon_1 + \epsilon_2 - \frac{16}{15}\epsilon_1\epsilon_2$.

When ϵ is small, second-order terms can be neglected.

For example, in Matrix (b) in Fig. 6, a Pauli error $W \in \{X, Y, Z\}$ at $D_1^{(1)}$ is equivalent to a Pauli error W at $D_2^{(1)}$. Therefore, these two locations are degenerate and can be merged into a single location.

Corollary 7. The ancilla preparation error location and the measurement error location in a raw stabilizer measurement circuit are degenerate.

According to Lemma 6 and Corollary 7, we derive Matrix (c) by deleting columns from Matrix (b) in Fig. 6.

C. Probabilistic Error Consolidation

In the previous subsection, we discussed how two degenerate error locations can be merged into a single error location. However, in many cases, error locations of different types may produce degenerate errors, but these locations cannot be directly merged. For example, a CNOT gate may produce degenerate errors with idle qubit errors, and two different CNOT gates might result in the same degenerate errors.

To address this, we propose probabilistic error consolidation by adjusting the initial error distributions so that one representative degenerate location is assigned the combined probability of two errors, while the other is set to zero probability. In this case, the two errors are said to be *probabilistically consolidated*. The key idea is that BP can effectively accommodate flexible input distributions.

Example 1. Consider Matrix (c) in Fig. 5.

- 1) (identical single-qubit columns) The errors IX, IZ, IY at $C_{2,1}^{(1)}$ can be probabilistically consolidated with errors

X, Y, Z at $D_1^{(2)}$. Similarly, the errors IX, IZ, IY at $C_{1,2}^{(1)}$ are degenerate with the errors X, Y, Z at $D_2^{(2)}$, which is also degenerate with $D_1^{(2)}$. As a result, these errors can all be probabilistically consolidated. The corresponding columns in Matrix (c) are highlighted in red.

- 2) The errors XI at $C_{1,1}^{(1)}$ and $C_{1,2}^{(1)}$ can be probabilistically consolidated with the bit-flip error at $m_1^{(1)}$. The corresponding components in Matrix (c) are highlighted in green.
- 3) The error ZI at $C_{1,1}^{(1)}$ and the errors IZ at $C_{1,2}^{(1)}$, $C_{2,1}^{(1)}$, $C_{2,2}^{(1)}$, and $C_{1,1}^{(2)}$ can be probabilistically consolidated with the error Z at $D_1^{(2)}$. Note that if errors IZ at $C_{1,2}^{(1)}$ and $C_{2,1}^{(1)}$ have already been probabilistically consolidated with error Z at $D_1^{(2)}$ as in 1), they can be skipped in subsequent steps. The corresponding components in Matrix (c) are highlighted in blue. The components highlighted in magenta are interpreted as both blue and red.
- 4) The error ZI at $C_{1,2}^{(1)}$ can be ignored as it is degenerate to no error.

Note that these probabilistic error consolidations can be implemented by checking their error syndromes from the generalized check matrix and their residual errors, without examining the syndrome circuit.

Next, we propose a simple procedure for consolidating error distributions based on the binary representation of the generalized check matrix. A conventional check matrix for an n -qubit quantum stabilizer code is a binary matrix where each stabilizer is represented by mapping single-qubit Pauli operators I, X, Z, Y to two binary bits: $(0|0), (1|0), (0|1), (1|1)$, respectively. In a similar fashion, a generalized check matrix can be represented in binary, where two-qubit Pauli operators are mapped to 4-bit strings, with each bit column corresponding to either a Pauli X or Z variable.

Our method for consolidating error distributions begins by merging degenerate error locations using Lemma 6. If a higher-order error variable partially shares degeneracy with a lower-order variable, it is decomposed into multiple lower-order variables. These degenerate lower-order variables are then merged. For example, a 16-ary two-qubit Pauli variable can be decomposed into either two quaternary variables or four binary variables. If the two quaternary variables are degenerate with others, they are merged first. If a quaternary variable is partially degenerate with a binary variable, it will be split into two binary variables, and the degenerate binary errors will be merged accordingly. In particular, if a 16-ary Pauli error is partially degenerate with a single-qubit X or Z error, it will be decomposed into one 8-ary variable and one binary variable.

For this purpose, each two-qubit Pauli error with a depolarizing rate ϵ can be decomposed as two independent single-qubit Pauli errors, each with an error rate of $4\epsilon/5$, or by four independent XI, IX, ZI , and IZ error variables, each with an error rate of $8\epsilon/15$. This holds because $\Pr(W_1, W_2) = \epsilon/15$ for any non-identity $(W_1, W_2) \in \{I, X, Y, Z\}^2$. Therefore, $\Pr(W_1 \neq I) = 12\epsilon/15$ and $\Pr(W_1 = X) = 8\epsilon/15$. Similarly, a single-qubit Pauli error with a depolarizing rate ϵ can be approximated by two independent X and Z error variables,

each with a rate of $2\epsilon/3$. After this decomposition, Lemma 6 is applied to merge degenerate quaternary or binary error variables. This entire procedure is summarized in Algorithm 2.

Algorithm 2 : Probabilistic error consolidation

Input: A syndrome extraction circuit \mathfrak{M} , an $M \times N$ generalized check matrix \mathcal{H} over a mixed alphabet of symbols from $\{I, X, Y, Z\}$, $\{I, X, Y, Z\}^2$, and $\{0, 1\}$, and initial error rates $\epsilon_1, \dots, \epsilon_N$.

Steps:

- 1: Merge error locations of the same type following Lemma 6. An error location is considered nontrivial if it has a nonzero error rate.
 - 2: Identify whether each active 16-ary error variable is degenerate with any quaternary error variable. If it is, decouple the 16-ary error variable into two quaternary error variables and merge the degenerate error variables.
 - 3: Identify whether each 16-ary error variable is degenerate with any binary error variable. If so, decompose the 16-ary error variable into one of the following configurations, depending on how many binary variables from the 16-ary variable need to be merged with other binary variables: (a) one 8-ary error variable and one binary error variable, (b) one quaternary error variable and two binary error variables, or (c) four binary error variables. Then, merge the degenerate error variables.
 - 4: Identify whether each 4-ary error variable is degenerate with any binary error variable. If it is, decouple the 4-ary error variable into two binary error variables and merge the degenerate error variables.
 - 5: Return the updated error distributions for each column.
-

Proposition 8. Algorithm 2 generates distributions for 16-ary, 8-ary, quaternary, and binary error variables at all locations, which can be used for initializing the FTBP error distribution.

As will be shown in Section VI, this error consolidation procedure, which decouples correlations in the Pauli operators, not only reduces the excess columns in the matrix but also decreases the number of short cycles in the generalized check matrix. This reduction in short cycles helps improve the error floor performance in BP decoding.

Additionally, we can use another approximation by first decomposing the 16-ary variables into quaternary variables, which simplifies the decoding complexity in FTBP.

Proposition 9. A two-qubit gate error location $C_{i,j}$ can be approximated by two single-qubit error variables $C_{i,j}^a$ and $C_{i,j}^d$ for ancilla and data qubits, respectively. In Algorithm 2, all 16-ary variables are first decomposed into two quaternary variables before step 2, and steps 2 and 3 are skipped. The resulting quaternary and binary error distributions can then be used to initialize the FTBP error distribution.

Figure 7 illustrates the Tanner graph induced from Matrix (c) in Fig. 6, using the approximation in Proposition 9. If each pair of $C_{i,j}^a$ and $C_{i,j}^d$ at round ℓ is integrated into a 16-

ary error variable node, this forms the Tanner graph described in Proposition 8.

In summary, all the techniques discussed in this section can be employed to reduce problem complexity in advance, without increasing the instantaneous decoding complexity.

V. LIFETIME OF A QUANTUM MEMORY

The simulation of a quantum memory begins with a noiseless encoded state and undergoes continuous syndrome extraction. After collecting syndromes over a window of r rounds, a decoding process is applied to determine the correction operator. However, residual data errors may remain after correction and carry over to the next cycle of error correction.

Definition 10. The *lifetime* of the memory is the average number of rounds it survives before a logical error occurs, and the *logical error rate* is the reciprocal of this lifetime.

To estimate the lifetime, both a virtual and an actual decoder are employed, as in [42, Algorithm 1]. Given r rounds of error syndromes, virtual decoding is first performed to assess whether the memory remains functional, assuming that an additional round of perfect syndromes is provided. If any logical errors are detected, the memory is declared dead. Otherwise, the memory is considered alive. If the memory is still functional after this check, actual decoding is performed based on the r rounds of syndrome extraction. This process is repeated until a logical error is detected, at which point the memory is considered dead.

In the example shown in Fig. 6, an additional round of perfect syndrome extraction is included to illustrate the process of virtual decoding.

A. Adaptive sliding window

Next, we consider improving FTBP decoding performance for a fixed-size decoding window. Since errors carry over between rounds of syndrome extraction, using non-overlapping decoding windows may degrade performance by neglecting these cross-boundary error correlations.

To address this issue, a sliding window scheme is proposed in [13]. For a window size of r syndrome extraction rounds, a fixed window offset of $r/2$ is suggested. In this method, r rounds of syndrome extraction are performed first, followed by a decoding process. Error correction is applied only to the first $r/2$ rounds of error locations, while the remaining $r/2$ rounds of syndromes are carried forward to the next error correction cycle. Subsequently, another $r/2$ rounds of syndrome extraction are performed, and the remaining $r/2$ rounds from the previous cycle are decoded alongside the newly acquired $r/2$ rounds. This iterative procedure allows for continuous error correction while maintaining manageable decoding complexity.

Note that in each window, errors occurring in the first $r/2$ rounds may be correlated with errors in the remaining $r/2$ rounds. This makes decoding with a fixed window offset suboptimal, as these correlations are not taken into account.

In practice, additional information about the occurred errors can be leveraged to improve decoding performance. In the

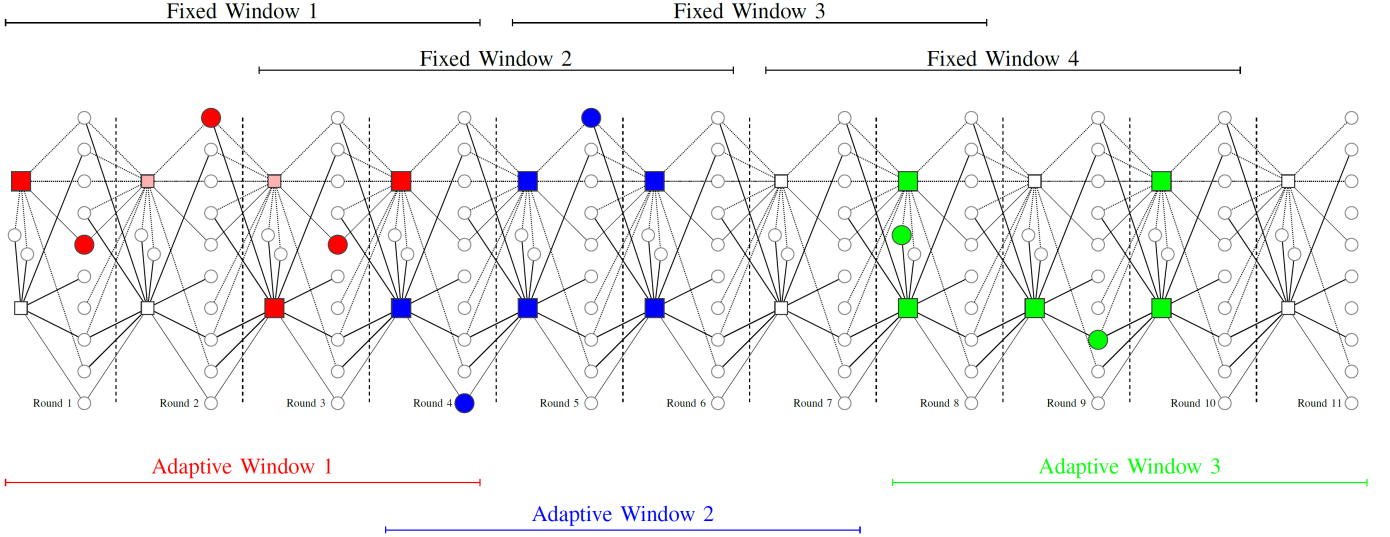


Fig. 8. A space-time Tanner graph corresponding to Matrix (c) in Fig. 6 with 11 rounds of syndrome extraction, extending the Tanner graph in Fig. 7. The variable nodes corresponding to nontrivial entries for a given set of errors are enlarged and highlighted in various colors. The check nodes connected to these variable nodes are similarly highlighted. The two check nodes in pink are not enlarged because their syndrome bits are 0. The fixed window scheme with four rounds is illustrated at the top, while the sliding window scheme is depicted at the bottom. Error correction is applied every two rounds.

context of a space-time Tanner graph, we say that two error locations are *connected* if their corresponding variable nodes are linked through a common check node. Given an estimated error from FTBP decoding, if there is a series of consecutive error locations connected to some error locations in the first half of the window, these errors are likely correlated and should be handled together. In such cases, the window offset should be adjusted accordingly. We propose an adaptive sliding window procedure with the following modifications to the original sliding window method.

Proposition 11. (Adaptive Sliding Window) Suppose that an error estimate for a decoding window is generated by FTBP.

- 1) Error correction is always applied to locations in the first half of the window.
- 2) Additionally, error locations connected to the first half of the window will also be corrected (even if these connections are near the window boundary).
- 3) Update the corresponding syndromes after applying the error correction.
- 4) The first uncorrected error location in the second half of the window will mark the starting point for the next window.

For illustration, a space-time Tanner graph corresponding to Matrix (c) in Fig. 6 is shown in Fig. 8. For a given set of errors highlighted in different colors, the check nodes with nontrivial syndromes are also marked in the corresponding colors. The sliding window procedure with a fixed window offset is demonstrated at the top of the Tanner graph, where each window covers four rounds of syndrome extraction with an offset of two rounds. Given these windows, As seen, several nontrivial connected errors span across these decision boundaries, such as the red errors occurring in the second and third rounds, positioned at the boundary between Fixed Window 1 and Fixed Window 2.

Our adaptive windows are shown at the bottom of the Tanner graph in Fig. 8, with adaptive window offsets. In Adaptive Window 1, if the red errors are decoded, they will be fully corrected since they are connected and span the first half of the window. However, the blue check node at Round 4 might lead to a decoded error that connects to other error nodes outside the current window. If this decoded error is not connected to errors within the first half of the window, it will not be corrected and will be deferred to the next decoding window.

Using the adaptive sliding window procedure from Proposition 11, the adaptive windows more effectively group errors into three sets of connected errors, resulting in more accurate error correction.

The adaptive window scheme in Proposition 11 shows improved performance in our simulations when the window size is set to $r = O(d)$ rounds of syndrome extraction, as will be demonstrated in the next section.

VI. SIMULATION RESULTS

In this section, we simulate the lifetime of a quantum memory protected by rotated toric codes, rotated 6.6.6 toric color codes, and twisted XZZX toric codes, all decoded using FTBP.

The parameter α in FTBP controls the step size in message passing, similar to MBP [35]. If a sequence of α values can be tested and an optimal α^* is adaptively selected, the decoder is referred to as FTBP(α^*), detailed in Appendix A.

In the following simulations, we consider equal error rates ϵ for data Pauli errors, syndrome bit errors, ancilla initialization errors, and two-qubit gate errors. The simulations use a maximum number of iterations $T_{\max} = 150$ and follow a serial message update schedule, as described in [34], [35]. We simulate FTBP(α^*) with $\alpha^* \in \{1, 0.99, \dots, 0.4\}$.

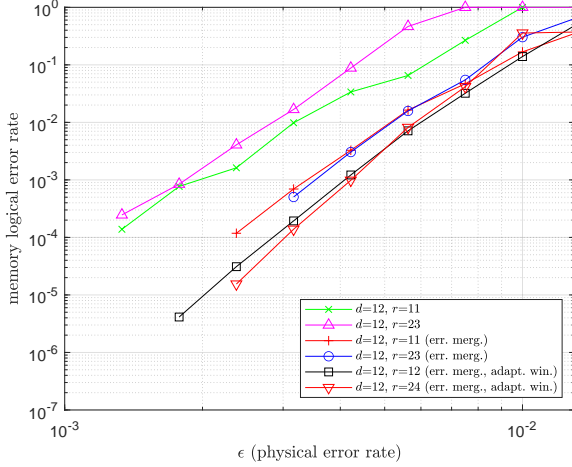


Fig. 9. Performance of $\text{FTBP}_4(\alpha^*)$ decoding on the $[[144, 2, 12]]$ rotated toric code with adaptive sliding windows and probabilistic error consolidation.

For clarity, we denote the decoder using the quaternary approximation from Proposition 9 as $\text{FTBP}_4(\alpha^*)$, while the decoder utilizing Proposition 8 is referred to as $\text{FTBP}_{16}(\alpha^*)$.

In the following simulation results, for a code with distance d , a bold dashed line representing a curve $a\epsilon^{t+1}$ is plotted, where $t = \lfloor \frac{d-1}{2} \rfloor$, and a is a scalar used to align it with the code's performance curve. This dashed line characterizes the error floor performance of the code.

The error threshold refers to the critical physical error rate below which a family of quantum error correction codes can effectively correct errors by increasing the code length. For a family of topological codes, the threshold is approximately located where the logical error rate performance curves for different code distances intersect. Since we are limited to simulating codes of finite sizes, we use the finite-size scaling ansatz [52], [53] to estimate the error thresholds of the topological code families considered in this paper (see Appendix D).

A. Probabilistic error consolidation and adaptive sliding window techniques

First, we demonstrate the effects of probabilistic error consolidation (Lemma 6 and Algorithm 2) and adaptive sliding windows (Proposition 11) on FTBP decoding of the $[[144, 2, 12]]$ rotated toric code. The performance results for various cases are shown in Fig. 9.

We first construct a generalized check matrix for the $[[144, 2, 12]]$ code using Lemma 5 with $r \approx d$. FTBP on the decoding problem induced by this generalized check matrix does not achieve the desired performance. Increasing the number of syndrome extraction rounds from 11 to 23 (i.e., $r > d$) does not improve the performance and may even lead to degradation.

By applying the probabilistic error consolidation techniques from Lemma 6, Algorithm 2, and Proposition 8, which adjust the corresponding error distributions, the FTBP_{16} decoding performance is significantly improved, as shown in

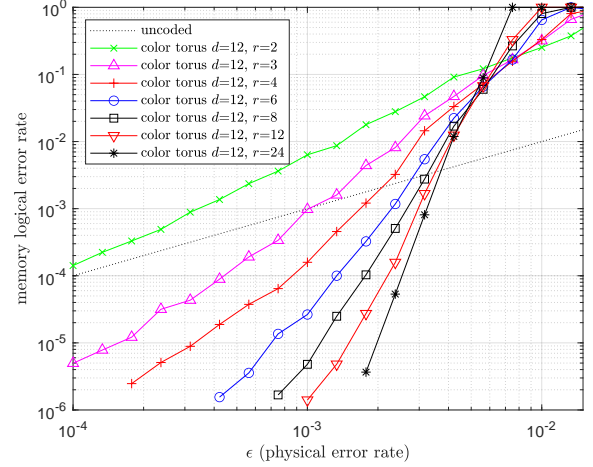


Fig. 10. $\text{FTBP}_4(\alpha^*)$ decoding performance on the $[[162, 4, 12]]$ rotated toric color code for different numbers of syndrome extraction rounds.

Fig. 9. However, increasing the number of syndrome extraction rounds beyond d still does not provide additional gains.

When both adaptive sliding windows and probabilistic error consolidation techniques are used together, performance further improves, with additional benefits observed from increasing the syndrome extraction rounds beyond d in the low logical error rate regime.

Consequently, in the following simulations, we will employ both probabilistic error consolidation and adaptive sliding windows techniques.

B. Size of a decoding window

In general, a generalized check matrix derived from a larger number of syndrome extraction rounds enhances circuit-level decoding, enabling the underlying stabilizer code to achieve its full error-correction potential by correcting up to $\lfloor (d-1)/2 \rfloor$ errors, where d is the minimum distance of the code. However, increasing the number of syndrome extraction rounds also raises the decoding complexity. It is believed that $O(d)$ rounds of syndrome extraction are sufficient to achieve good decoding performance [13].

We examine the impact of increasing syndrome extraction rounds within a decoding window on the quantum memory lifetime. Figure 10 shows the FTBP decoding performance for the $[[162, 4, 12]]$ rotated 6.6.6 toric color code, comparing different numbers of syndrome extraction rounds (r) in a decoding window.

To achieve this, we construct generalized check matrices for various values of r using Lemma 5. Additionally, we apply probabilistic error consolidation techniques from Lemma 6, Algorithm 2, and Proposition 9 to enhance performance.

At higher physical error rates, using a smaller number of r tends to yield better performance. This is because a larger r value generates a more extensive space-time Tanner graph, which complicates the BP decoding process due to the increased number of possible error combinations. Moreover, at high physical error rates, a larger r may result in excessive error accumulation, leading to a logical error.

Conversely, in low-error-rate regions, decoding performance improves as r increases, eventually saturating at around $r \approx 2d$. Further simulations on toric codes, toric color codes, and twisted XZZX toric codes (detailed in Appendix B) show that for twisted XZZX toric codes, around $2d$ rounds of syndrome extraction are required for optimal performance. For toric codes, performance saturates at $r \approx d$. Increasing the number of rounds beyond this enhances performance, especially in low-error-rate regions, although the threshold behavior remains mostly unchanged. Thus, choosing d to $2d$ rounds of syndrome extraction per decoding window is sufficient for topological codes with distance d .

In the following simulations for a rotated toric code with distance d , we consider the pointwise minimum of the performance curves at each error rate, using round numbers ranging from 3 to d to identify the optimal decoding performance. For the rotated color code or twisted XZZX toric code, we follow a similar approach but with more rounds, ranging from 3 to $2d$. For example, we will use the lower envelope of the curves in Fig. 10 to represent the $\text{FTBP}_4(\alpha^*)$ decoding performance of the rotated 6.6.6 toric color code with $d = 12$.

C. Quantum memory with rotated toric codes

We simulate the quantum memory using the family of $[[d^2, 2, d]]$ rotated toric codes for $d \leq 12$ and plot the results in Fig. 11. In these simulations, we apply the probabilistic error consolidation techniques from Lemma 6, Algorithm 2, and Proposition 8. For each error rate, the best-performing curve is selected by choosing the pointwise minimum across various round numbers, ranging from 3 to d .

Using $d = 6, 8, 10, 12$, the finite-size scaling ansatz estimates a threshold of 0.75% for rotated toric codes (see Appendix D), which aligns with the observed intersection of the performance curves in Fig. 11. This result is comparable to the thresholds obtained with MWPM in [14], [16], [55], while using the more efficient FTBP algorithm with adaptive sliding window decoding in lifetime simulations.

For reference, a threshold of 0.68% for 2D surface codes was reported in [46] using MWPM with parallel sliding window decoding, where the decoding window spans $\frac{3d}{2}$ syndrome extraction rounds.

Additionally, we compare the decoders FTBP_4 and FTBP_{16} , which use probabilistic error consolidation techniques based on Proposition 9 and Proposition 8, respectively. The simulation results show that both decoders perform similarly on the rotated toric codes.

D. Quantum memory with rotated 6.6.6 toric color codes

Consider the family of $[[\frac{9}{8}d^2, 4, d]]$ rotated 6.6.6 toric color codes for $d = 4, 8, 12$. We apply FTBP decoding to these codes using probabilistic error consolidation and adaptive sliding windows, with the simulation results shown in Fig. 12. The curves are generated using either $\text{FTBP}_4(\alpha^*)$ or $\text{FTBP}_{16}(\alpha^*)$, depending on which performs better across different regions of the logical error rate. It is observed that $\text{FTBP}_4(\alpha^*)$ performs better in low error rate regions, while $\text{FTBP}_{16}(\alpha^*)$ excels near the error threshold. This is because $\text{FTBP}_{16}(\alpha^*)$ captures more

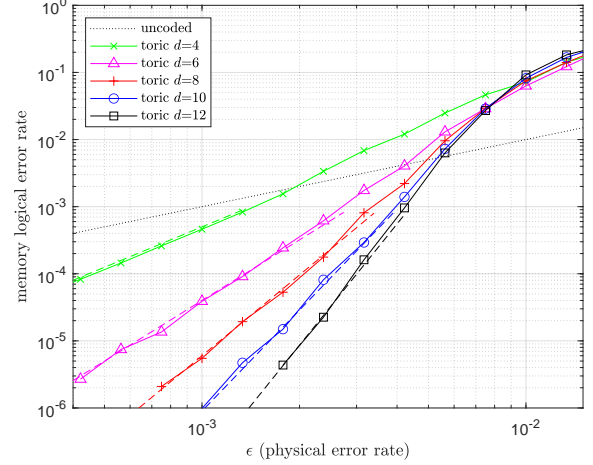


Fig. 11. $\text{FTBP}_{16}(\alpha^*)$ decoding performance for the $[[d^2, 2, d]]$ rotated toric codes with $d \leq 12$.

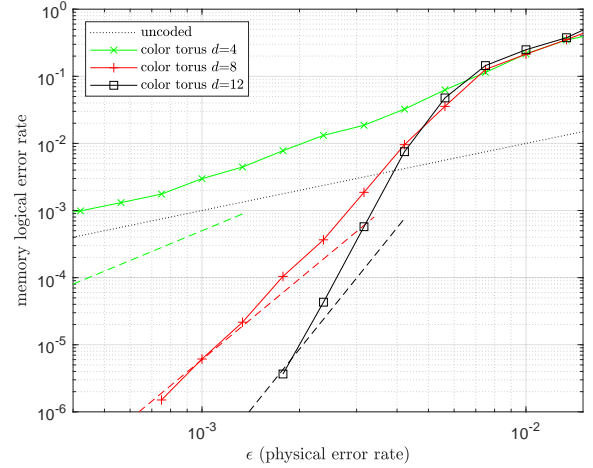


Fig. 12. $\text{FTBP}(\alpha^*)$ decoding performance for the $[[\frac{9}{8}d^2, 4, d]]$ rotated 6.6.6 toric color codes with $d = 4, 8, 12$. The curves are generated using either $\text{FTBP}_4(\alpha^*)$ or $\text{FTBP}_{16}(\alpha^*)$, depending on which performs better across different regions of the logical error rate. The dashed lines are replicated from the toric code case (Fig. 11) for comparison purposes.

error correlations, which is crucial at high error rates, whereas $\text{FTBP}_4(\alpha^*)$ is more effective because its Tanner graph has fewer short cycles, which are more impactful at low error rates. Additional simulations are provided in Appendix C.

The performance curves for $d = 8$ and $d = 12$ intersect approximately between 0.4% and 0.5%, as shown in Fig. 12. Using $d = 8$ and $d = 12$, the scaling ansatz estimates a threshold of 0.59% (see Appendix D). Therefore, we expect the $\text{FTBP}(\alpha^*)$ decoding threshold for the rotated 6.6.6 toric color codes to lie between 0.4% and 0.59%. Note that the color code with $d = 4$ exhibits poor performance. This is because it the stabilizers that need to be measured have weight six, and raw syndrome extraction is not fault-tolerant, leading to more errors than it can handle.

Unlike the rotated toric codes, these rotated color codes show improved performance with $\text{FTBP}_4(\alpha^*)$ when the number of syndrome extraction rounds in a decoding window

increases from d to $2d$, particularly in the low logical error rate region. Additional simulations are provided in Appendix B.

Compared to the rotated toric codes, the rotated color codes exhibit a delayed waterfall roll-off. In Fig. 11, the performance curve for the rotated toric code with $d = 12$ aligns with the error floor performance at a logical error rate around 10^{-4} . For comparison, the dashed lines representing the error floors for toric codes with $d = 4, 8, 12$ in Fig. 11 are also shown in Fig. 12. In contrast, the performance curve for the rotated 6.6.6 toric color code with $d = 12$ has a steeper slope and does not align with the error floor by 5×10^{-5} . Consequently, the rotated color codes demonstrate better error-floor performance compared to the rotated toric codes.

For comparison, the $[[\frac{3d^2+1}{4}, 1, d]]$ triangular 6.6.6 color codes, which achieve a threshold of 0.2% using the restriction decoder with flagged syndrome extraction [16] when adopting a lower measurement error rate of $2\epsilon/3$. We can compare the $[[72, 4, 8]]$ 6.6.6 toric color code with the $[[61, 1, 9]]$ triangular 6.6.6 color code. Both codes have similar distances but their code rates differ: $1/18$ for the $[[72, 4, 8]]$ code and $1/61$ for the $[[61, 1, 9]]$ code. The $[[61, 1, 9]]$ code demonstrates an X -logical error rate of approximately 3×10^{-3} at the physical error rate of 10^{-3} [16, Figure 10], while the $[[72, 4, 8]]$ code achieves a much lower logical error rate of 10^{-5} at the same physical error rate of 10^{-3} as shown in Fig. 12. In fact, FTBP decoding of the $[[72, 4, 8]]$ code results in a logical error rate even lower than that of the $d = 15$ triangular 6.6.6 color code [16, Figure 10]. Thus FTBP decoding for the $[[72, 4, 8]]$ 6.6.6 toric color code exhibits significantly improved error performance and a higher code rate.

For reference, a threshold of 0.1% to 0.143% has been reported for the $[[\frac{(d-1)^2}{2} + d, 1, d]]$ 2D 4.8.8 color codes [11] using $d \leq 9$ [15], [59] with modified MWPM decoders. Our FTBP(α^*) decoder not only achieves a better threshold value for the rotated 6.6.6 toric color codes but also exhibits superior error-floor performance.

For example, consider comparing the $[[72, 4, 8]]$ 6.6.6 toric color code with the $[[41, 1, 9]]$ 4.8.8 color code. Although these two codes have similar distances, the $[[72, 4, 8]]$ code offers a higher code rate of $1/18$. To make a fair comparison, we could use two codewords of the $[[41, 1, 9]]$ code, which would require 82 physical qubits to protect two logical qubits. Modified MWPM decoding for the $[[41, 1, 9]]$ code results in a memory lifetime of 10^2 rounds at a physical error rate of 10^{-3} [59, Fig. 14], corresponding to a logical error rate of 10^{-2} . Thus, simulating two codewords would yield a worse logical error rate.

In contrast, FTBP(α^*) decoding for the $[[72, 4, 8]]$ 6.6.6 toric color code achieves a memory lifetime of 10^5 rounds at the same physical error rate of 10^{-3} , corresponding to a logical error rate of 10^{-5} , which is three orders of magnitude better.

E. Quantum memory with twisted XZZX toric codes

Our decoding algorithm is also applicable to non-CSS codes. We simulate the $[[\frac{(d^2+1)}{2}, 1, d]]$ twisted XZZX toric codes. The stabilizers that need to be measured for these codes

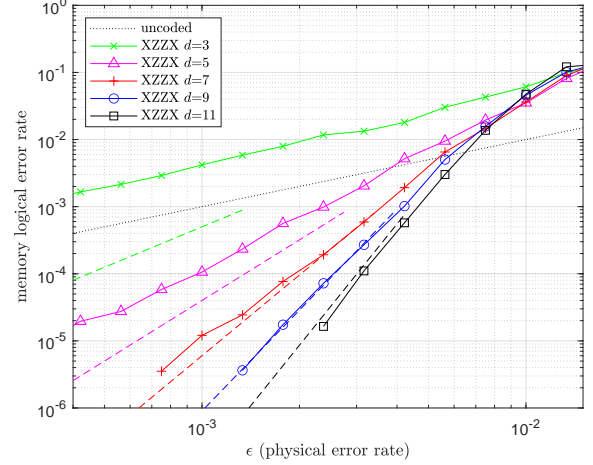


Fig. 13. FTBP $_{16}(\alpha^*)$ decoding performance for the twisted XZZX toric codes with $d \leq 12$. The dashed lines are replicated from the toric code case (Fig. 11) for comparison purposes.

have a weight of 4, similar to toric codes. We use a cross-type order for raw stabilizer measurements. Given the similarity to toric codes, we only consider FTBP $_{16}(\alpha^*)$. The simulation results are shown in Fig. 13.

However, unlike toric codes, the XZZX stabilizers can lead to more complex error propagation behaviors in the syndrome extraction circuit. Raw stabilizer measurements are not effective for twisted XZZX toric codes with $d \leq 7$. Nevertheless, for larger distances $d \geq 9$, with up to approximately $2d$ rounds of syndrome measurements in a decoding window, the FTBP $_{16}(\alpha^*)$ decoding performance for twisted XZZX toric codes is comparable to that of rotated toric codes (see Appendix B).

Using $d = 7, 9, 11$, the finite-size scaling ansatz estimates a threshold of 0.87% for twisted XZZX toric codes (see Appendix D). However, the performance curves appear to intersect around 0.75%–0.8% in Fig. 13. Thus we expect the FTBP $_{16}(\alpha^*)$ decoding threshold for twisted XZZX toric codes lies between 0.75% and 0.87%.

VII. CONCLUSION

In conclusion, we have proposed methods for performing fault-tolerant belief propagation decoding on general quantum codes, extending the quantum data-syndrome code framework to handle circuit-level noise. Several techniques were introduced to improve decoding performance in quantum memory lifetime simulations, including the use of sparse generalized check matrices, probabilistic error consolidation, and adaptive sliding windows. Our approach is versatile, applying to general topological codes, including non-CSS codes, which are typically among the most challenging to decode. Furthermore, this discussion can be easily extended to accommodate other syndrome extraction procedures.

In our simulations, the rotated toric and twisted XZZX toric codes exhibited higher error thresholds, while the rotated color codes showed a lower error floor. We also demonstrated that FTBP decoding outperforms the modified MWPM decoder,

achieving a higher threshold on the rotated 6.6.6 color codes compared to the 2D 4.8.8 color codes, while operating with significantly lower complexity.

Note that the generalized check matrix constructed using Lemma 5 may resemble the decoding graph used in MWPM for toric codes [13]. However, our approach involves mixed variable nodes, and we do not utilize separate primal and dual lattices for decoding X and Z errors. Additionally, our derivation employs the method of syndrome assignment from coding theory, emphasizing a preference for sparser matrices.

For FTBP, two-qubit gate errors are treated as 16-ary errors. However, in our approach, some correlations are disregarded to reduce degeneracy and minimize short cycles in the Tanner graph. Further research is needed to effectively incorporate these correlations while maintaining efficient FTBP decoding to enhance overall decoding performance.

The simulation results could be further optimized by incorporating additional techniques, such as more syndrome extraction rounds in a decoding window, fixed initialization in BP [35], [42], [60] or expanding the range of the parameter α in FTBP. However, fixed initialization requires extensive pre-simulations for parameter tuning, which we did not explore in our results due to the already high simulation complexity of our current approach.

In our simulations, a serial schedule for BP was employed. Future work could explore the effects of different probabilistic error consolidation sequences and BP scheduling strategies. Additionally, BP scheduling may influence the optimal sequence of syndrome measurements for each stabilizer. Notably, we observed that a cross-type sequence leads to improved FTBP decoding performance for topological codes under a serial schedule.

For implementation, an efficient procedure can be constructed using a matrix of row operations to convert location errors into residual data errors. As a result, it becomes unnecessary to track the error evolution throughout the syndrome measurement circuit.

REFERENCES

- [1] P. W. Shor, "Scheme for reducing decoherence in quantum computer memory," *Phys. Rev. A*, vol. 52, pp. 2493–2496, 1995.
- [2] A. M. Steane, "Error correcting codes in quantum theory," *Phys. Rev. Lett.*, vol. 77, p. 793, 1996.
- [3] A. R. Calderbank and P. W. Shor, "Good quantum error-correcting codes exist," *Phys. Rev. A*, vol. 54, p. 1098, 1996.
- [4] E. Knill and R. Laflamme, "Theory of quantum error-correcting codes," *Phys. Rev. A*, vol. 55, pp. 900–911, 1997.
- [5] D. Gottesman, "Stabilizer codes and quantum error correction," Ph.D. dissertation, California Institute of Technology, CA, USA, 1997.
- [6] D. P. DiVincenzo and P. W. Shor, "Fault-tolerant error correction with efficient quantum codes," *Phys. Rev. Lett.*, vol. 77, no. 15, pp. 3260–3263, 1996.
- [7] D. Gottesman, "Theory of fault-tolerant quantum computation," *Phys. Rev. A*, vol. 57, p. 127, 1998.
- [8] D. Aharonov and M. Ben-Or, "Fault-tolerant quantum computation with constant error rate," *SIAM J. Comput.*, 2008.
- [9] S. Bravyi and A. Kitaev, "Universal quantum computation with ideal Clifford gates and noisy ancillas," *Phys. Rev. A*, vol. 71, p. 022316, 2005.
- [10] A. Y. Kitaev, "Fault-tolerant quantum computation by anyons," *Ann. Phys.*, vol. 303, no. 1, pp. 2–30, 2003.
- [11] H. Bombin and M. A. Martin-Delgado, "Topological quantum distillation," *Phys. Rev. Lett.*, vol. 97, p. 180501, 2006.
- [12] —, "Optimal resources for topological two-dimensional stabilizer codes: Comparative study," *Phys. Rev. A*, vol. 76, p. 012305, 2007.
- [13] E. Dennis, A. Kitaev, A. Landahl, and J. Preskill, "Topological quantum memory," *J. Math. Phys.*, vol. 43, no. 9, pp. 4452–4505, 2002.
- [14] R. Raussendorf and J. Harrington, "Fault-tolerant quantum computation with high threshold in two dimensions," *Phys. Rev. Lett.*, vol. 98, p. 190504, 2007.
- [15] A. M. Stephens, "Efficient fault-tolerant decoding of topological color codes," 2014, e-print at <https://arxiv.org/abs/1402.3037>.
- [16] C. Chamberland, A. Kubica, T. J. Yoder, and G. Zhu, "Triangular color codes on trivalent graphs with flag qubits," *New Journal of Physics*, vol. 22, no. 2, p. 023019, 2020.
- [17] D. J. C. MacKay, G. Mitchison, and P. L. McFadden, "Sparse-graph codes for quantum error correction," *IEEE Trans. Inf. Theory*, vol. 50, no. 10, pp. 2315–2330, 2004.
- [18] J.-P. Tillich and G. Zémor, "Quantum LDPC codes with positive rate and minimum distance proportional to the square root of the blocklength," *IEEE Trans. Inf. Theory*, vol. 60, no. 2, pp. 1193–1202, 2014.
- [19] A. A. Kovalev and L. P. Pryadko, "Quantum Kronecker sum-product low-density parity-check codes with finite rate," *Phys. Rev. A*, vol. 88, p. 012311, 2013.
- [20] D. Gottesman, "Fault-tolerant quantum computation with constant overhead," *Quantum Inf. Comput.*, vol. 14, no. 15–16, pp. 1338–1372, 2014.
- [21] P. Panteleev and G. Kalachev, "Degenerate quantum LDPC codes with good finite length performance," *Quantum*, vol. 5, p. 585, 2021.
- [22] H.-K. Lin and L. P. Pryadko, "Quantum two-block group algebra codes," *Phys. Rev. A*, vol. 109, p. 022407, 2024.
- [23] S. Bravyi, A. W. Cross, J. M. Gambetta, D. Maslov, P. Rall, and T. J. Yoder, "High-threshold and low-overhead fault-tolerant quantum memory," *Nature*, vol. 627, no. 8005, pp. 778–782, 2024.
- [24] B. M. Terhal, "Quantum error correction for quantum memories," *Rev. Mod. Phys.*, vol. 87, no. 2, pp. 307–346, 2015.
- [25] J. Edmonds, "Paths, trees, and flowers," *Can. J. Math.*, vol. 17, pp. 449–467, 1965.
- [26] R. Raussendorf, J. Harrington, and K. Goyal, "Topological fault-tolerance in cluster state quantum computation," *New J. Phys.*, vol. 9, no. 6, p. 199, 2007.
- [27] N. Delfosse and N. H. Nickerson, "Almost-linear time decoding algorithm for topological codes," *Quantum*, vol. 5, p. 595, 2021.
- [28] S. Huang, M. Newman, and K. R. Brown, "Fault-tolerant weighted union-find decoding on the toric code," *Physical Review A*, vol. 102, no. 1, p. 012419, 2020.
- [29] R. G. Gallager, *Low-Density Parity-Check Codes*, ser. no. 21 in Research Monograph Series. MIT Press, 1963. [Online]. Available: <https://doi.org/10.7551/mitpress/4347.001.0001>
- [30] R. Tanner, "A recursive approach to low complexity codes," *IEEE Trans. Inf. Theory*, vol. 27, no. 5, pp. 533–547, 1981.
- [31] J. Pearl, *Probabilistic reasoning in intelligent systems: networks of plausible inference*. Kaufmann, 1988.
- [32] F. R. Kschischang, B. J. Frey, and H.-A. Loeliger, "Factor graphs and the sum-product algorithm," *IEEE Trans. Inf. Theory*, vol. 47, no. 2, pp. 498–519, 2001.
- [33] D. Poulin and Y. Chung, "On the iterative decoding of sparse quantum codes," *Quantum Inf. Comput.*, vol. 8, pp. 987–1000, 2008.
- [34] K.-Y. Kuo and C.-Y. Lai, "Refined belief propagation decoding of sparse-graph quantum codes," *IEEE J. Sel. Areas Inf. Theory*, vol. 1, no. 2, pp. 487–498, 2020.
- [35] —, "Exploiting degeneracy in belief propagation decoding of quantum codes," *npj Quantum Inf.*, vol. 8, 2022, article no. 111. (See a complete version at <https://arxiv.org/abs/2104.13659>).
- [36] J. Roffe, D. R. White, S. Burton, and E. T. Campbell, "Decoding across the quantum low-density parity-check code landscape," *Phys. Rev. Res.*, vol. 2, p. 043423, 2020.
- [37] C.-F. Kung, K.-Y. Kuo, and C.-Y. Lai, "On belief propagation decoding of quantum codes with quaternary reliability statistics," in *Proc. IEEE Int. Symp. Top. Coding (ISTC)*, 2023, pp. 1–5.
- [38] Y.-J. Wang, B. C. Sanders, B.-M. Bai, and X.-M. Wang, "Enhanced feedback iterative decoding of sparse quantum codes," *IEEE Trans. Inf. Theory*, vol. 58, no. 2, pp. 1231–1241, 2012.
- [39] Z. Babar, P. Botsinis, D. Alanis, S. X. Ng, and L. Hanzo, "Fifteen years of quantum LDPC coding and improved decoding strategies," *IEEE Access*, vol. 3, pp. 2492–2519, 2015.
- [40] C.-Y. Lai and K.-Y. Kuo, "Log-domain decoding of quantum LDPC codes over binary finite fields," *IEEE Trans. Quantum Eng.*, vol. 2, 2021, article no. 2103615.

- [41] K.-Y. Kuo, I.-C. Chern, and C.-Y. Lai, “Decoding of quantum data-syndrome codes via belief propagation,” in *Proc. IEEE Int. Symp. Inf. Theory (ISIT)*, 2021, pp. 1552–1557.
- [42] K.-Y. Kuo and C.-Y. Lai, “Correcting phenomenological quantum noise via belief propagation,” *arXiv preprint arXiv:2310.12682*, 2023.
- [43] A. R. Calderbank, E. M. Rains, P. W. Shor, and N. J. A. Sloane, “Quantum error correction via codes over GF(4),” *IEEE Trans. Inf. Theory*, vol. 44, no. 4, pp. 1369–1387, 1998.
- [44] L. P. Pryadko, “On maximum-likelihood decoding with circuit-level errors,” *Quantum*, vol. 4, p. 304, 2020.
- [45] C. Gidney, “Stim: a fast stabilizer circuit simulator,” *Quantum*, vol. 5, p. 497, 2021.
- [46] X. Tan, F. Zhang, R. Chao, Y. Shi, and J. Chen, “Scalable surface-code decoders with parallelization in time,” *PRX Quantum*, vol. 4, no. 4, p. 040344, 2023.
- [47] L. Skoric, D. E. Browne, K. M. Barnes, N. I. Gillespie, and E. T. Campbell, “Parallel window decoding enables scalable fault tolerant quantum computation,” *Nat. Commun.*, vol. 14, no. 1, p. 7040, 2023.
- [48] A. Gong, S. Cammerer, and J. M. Renes, “Toward low-latency iterative decoding of QLDPC codes under circuit-level noise,” *arXiv preprint arXiv:2403.18901*, 2024.
- [49] A. A. Kovalev, I. Dumer, and L. P. Pryadko, “Design of additive quantum codes via the code-word-stabilized framework,” *Phys. Rev. A*, vol. 84, no. 6, p. 062319, 2011.
- [50] R. Sarkar and T. J. Yoder, “A graph-based formalism for surface codes and twists,” *Quantum*, vol. 8, p. 1416, 2024.
- [51] K.-Y. Kuo and C.-Y. Lai, “Comparison of 2D topological codes and their decoding performances,” in *Proc. IEEE Int. Symp. Inf. Theory (ISIT)*, 2022, pp. 186–191.
- [52] C. Wang, J. Harrington, and J. Preskill, “Confinement-Higgs transition in a disordered gauge theory and the accuracy threshold for quantum memory,” *Ann. Phys.*, vol. 303, no. 1, pp. 31–58, 2003.
- [53] J. W. Harrington, “Analysis of quantum error-correcting codes: symplectic lattice codes and toric codes,” Ph.D. dissertation, California Institute of Technology, CA, USA, 2004.
- [54] D. S. Wang, A. G. Fowler, and L. C. Hollenberg, “Surface code quantum computing with error rates over 1%,” *Phys. Rev. A*, vol. 83, p. 020302, 2011.
- [55] A. M. Stephens, “Fault-tolerant thresholds for quantum error correction with the surface code,” *Phys. Rev. A*, vol. 89, p. 022321, 2014.
- [56] M. A. Nielsen and I. L. Chuang, *Quantum Computation and Quantum Information*. Cambridge University Press, 2000.
- [57] A. Ashikhmin, C.-Y. Lai, and T. A. Brun, “Correction of data and syndrome errors by stabilizer codes,” in *Proc. IEEE Int. Symp. Inf. Theory (ISIT)*, 2016, pp. 2274–2278.
- [58] —, “Quantum data-syndrome codes,” *IEEE J. Sel. Areas Commun.*, vol. 38, no. 3, pp. 449–462, 2020.
- [59] D. S. Wang, A. G. Fowler, C. D. Hill, and L. C. L. Hollenberg, “Graphical algorithms and threshold error rates for the 2d color code,” *Quantum Inf. Comput.*, vol. 10, no. 9, pp. 780–802, 2010.
- [60] M. Hagiwara, M. P. C. Fossorier, and H. Imai, “Fixed initialization decoding of LDPC codes over a binary symmetric channel,” *IEEE Trans. Inf. Theory*, vol. 58, no. 4, pp. 2321–2329, 2012.

APPENDIX

A. Adaptive version of FTBP

The parameter α in FTBP (Algorithm 1) can be determined based on the mean row-weight, physical error rate, and some pre-simulations (refer to Fig.3 and Appendix B.1 in the arXiv version of [35]). For enhanced performance, the optimal value α^* can be adaptively selected. This adaptive algorithm, FTBP(α^*), builds upon the AMBP algorithms [35] and extends FTBP. The details of this algorithm are presented in Algorithms 3. Since BP typically converges in about $\log N$ iterations, selecting $T_{\max} = O(\log N)$ is generally sufficient. For the decrement sweep of $\alpha_1 > \alpha_2 > \dots > \alpha_\ell > 0$, a step size of 0.01 is sufficient because α controls the strength of message passing, and BP tends to converge within $O(\log N)$ iterations, making it relatively insensitive to changes in α . Additionally, multiple FTBP instances with different α values can be executed in parallel.

Algorithm 3 : FTBP(α^*)

Input: An $M \times N$ generalized check matrix \mathcal{H} over a mixed alphabet of symbols from $\{I, X, Y, Z\}$, $\{I, X, Y, Z\}^2$, and $\{0, 1\}$, an error syndrome vector $s \in \{0, 1\}^M$, an integer $T_{\max} > 0$, a sequence of ℓ parameters $\alpha_1 > \alpha_2 > \dots > \alpha_\ell > 0$, and initial LLRs $\Lambda_1, \dots, \Lambda_N$.

Initialization: Let $i = 1$.

- **BP Step:** Run FTBP($\mathcal{H}, s, T_{\max}, \alpha_i$, initial LLRs), which returns “CONVERGE” or “FAIL” with an error vector $\hat{\mathcal{E}}$ over $\{I, X, Y, Z\}, \{I, X, Y, Z\}^2, \{0, 1\}$.
- **Adaptive Check:**
 - If “CONVERGE”, output $\hat{\mathcal{E}}$ and $\alpha^* = \alpha_i$ and return “SUCCESS”;
 - Else, if $i < \ell$, update $i \leftarrow i + 1$ and repeat from the BP Step;
 - Else, return “FAIL”.

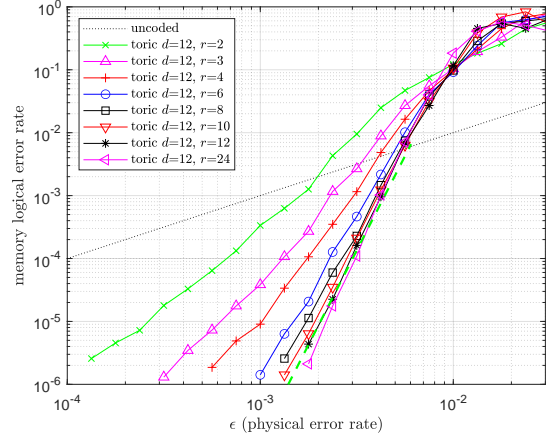


Fig. 14. FTBP₁₆(α^*) decoding performance on the $[[144, 2, 12]]$ rotated toric code for different numbers of syndrome extraction rounds. The bold dashed line represents the curve $a\epsilon^{t+1}$, where $t = \lfloor \frac{d-1}{2} \rfloor$ and a is a scalar chosen to align the curves for $r \approx d$.

B. Increasing the rounds of syndrome extraction in a decoding window

Figure 14 illustrates the FTBP decoding performance for the $[[144, 2, 12]]$ rotated toric code. As shown, decoding performance improves with the number of rounds (r) and begins to saturate around $r \approx d$. Similar trends are observed for the $[[72, 4, 8]]$ rotated 6.6.6 toric color code and the $[[41, 1, 9]]$ and $[[61, 1, 11]]$ twisted XZZX toric codes in Figs. 15, 16, and 17. However, for these codes, further improvements are still seen as r increases to $2d$.

Increasing the number of syndrome extraction rounds to twice the code distance further enhances decoding performance, particularly in low-error-rate regions. However, the threshold behavior remains largely unaffected. Therefore, d rounds of syndrome extraction in a decoding window is sufficient for a topological code with distance d .

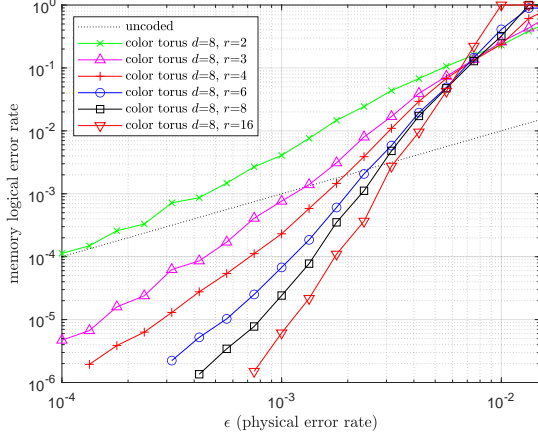


Fig. 15. FTBP(α^*) decoding performance on the $[[72, 4, 8]]$ rotated 6.6.6 toric color code for different numbers of syndrome extraction rounds.

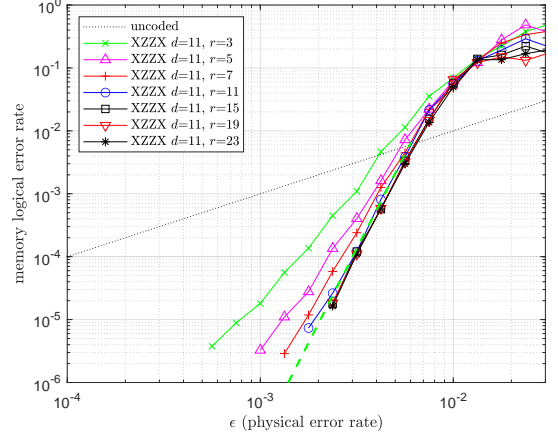


Fig. 17. FTBP₁₆(α^*) decoding performance on the $[[61, 1, 11]]$ twisted XZZX toric code for different numbers of syndrome extraction rounds.

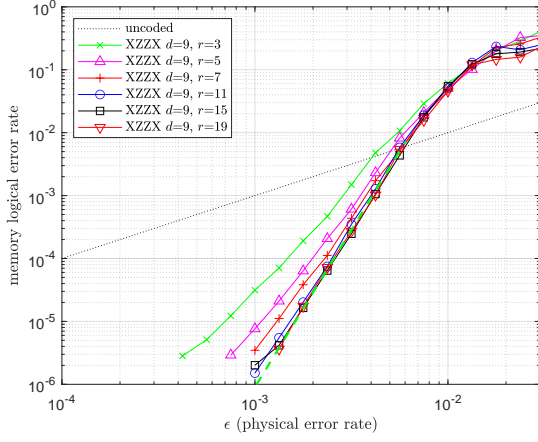


Fig. 16. FTBP₁₆(α^*) decoding performance on the $[[41, 1, 9]]$ twisted XZZX toric code for different numbers of syndrome extraction rounds.

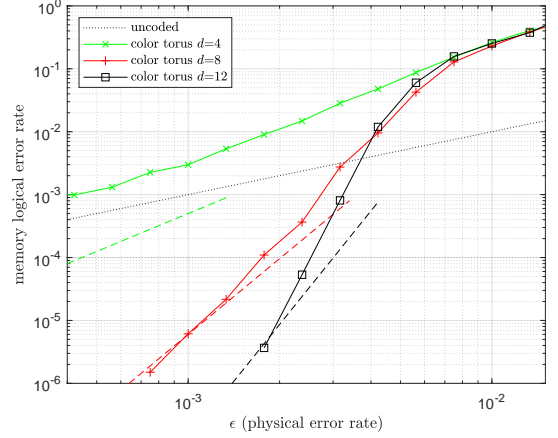


Fig. 18. FTBP₄(α^*) decoding performance for the rotated 6.6.6 toric color codes with $d = 4, 8, 12$.

C. FTBP₄(α^*) v.s. FTBP₁₆(α^*)

We compare the decoders FTBP₄ and FTBP₁₆, which use probabilistic error consolidation techniques based on Proposition 9 and Proposition 8, respectively. The simulation results show that both decoders perform similarly on the rotated toric codes.

However, the performance differs significantly for the rotated 6.6.6 toric color codes. It is observed that FTBP₄(α^*) performs better in low error rate regions, while FTBP₁₆(α^*) excels near the error threshold, as shown in Figs. 18 and 19. The dashed lines in each figure are replicated from the toric code case (Fig. 11) for comparison.

D. Error threshold estimates through finite-size scaling ansatz

We use the finite-size scaling ansatz [52], [53] to estimate the error thresholds of the topological code families considered in this paper, as we are limited to simulating codes of finite sizes. The ansatz assumes that the logical error rate $P_L(\epsilon, d)$

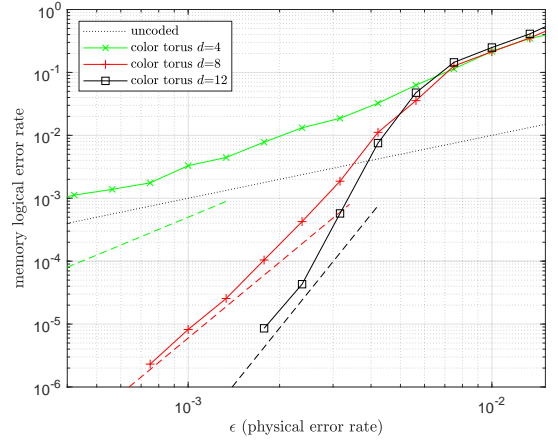


Fig. 19. FTBP₁₆(α^*) decoding performance for the rotated 6.6.6 toric color codes with $d = 4, 8, 12$.

for a code of distance d at depolarizing rate ϵ can be modeled

as:

$$P_L(\epsilon, d) = f(d^{-\nu}(\epsilon - \tau)),$$

where τ is the error threshold and ν is critical exponent that characterizes the scaling behavior near the threshold. The function $f(x)$ is a universal scaling function, and the simulation data will be fitted using a low-degree polynomial in x . For this analysis, we employ a degree-3 polynomial for the data fitting.

The rescaled FTBP₁₆(α^*) decoding threshold performance for the rotated toric codes is shown in Fig. 20 (a). Using $d = 4$ to 12, the ansatz estimates a threshold of 0.91%. In Fig. 11, the performance curves intersect around 0.75% to 0.8%, except for $d = 4$, which deviates the expected behavior of the ansatz model. Consequently, we exclude the $d = 4$ curve and obtain a more accurate threshold estimate of 0.75%, as shown in Fig. 20 (b).

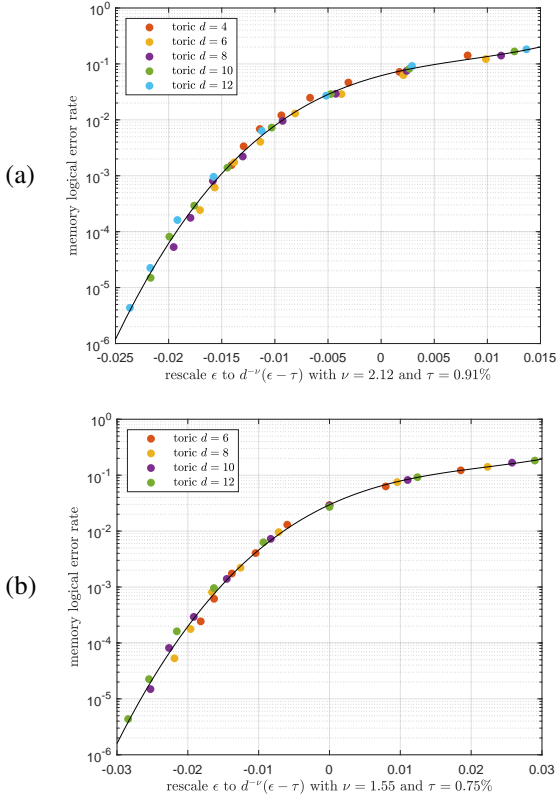


Fig. 20. Rescaled FTBP₁₆(α^*) decoding threshold performance for rotated toric codes with (a) $d = 4, 6, 8, 10, 12$ and (b) $d = 6, 8, 10, 12$.

For FTBP(α^*) decoding of the rotated 6.6.6 color toric codes, the ansatz estimates a threshold of 0.70% using $d = 4, 8, 12$, as shown in Fig. 21 (a). It is clear that the $d = 4$ curve is not effective for error correction as shown in Fig. 12. Excluding the $d = 4$ curve, the ansatz estimates a more accurate threshold of 0.59% using $d = 8$ and 12, as shown in Fig. 21 (b).

Similarly, the ansatz estimates a threshold of 0.91% for twisted XZZX toric codes using $d = 5, 7, 9, 11$, as shown in Fig. 22 (a). Excluding the $d = 5$ curve, the ansatz provides a more accurate threshold of 0.87%, as shown in Fig. 22 (b).

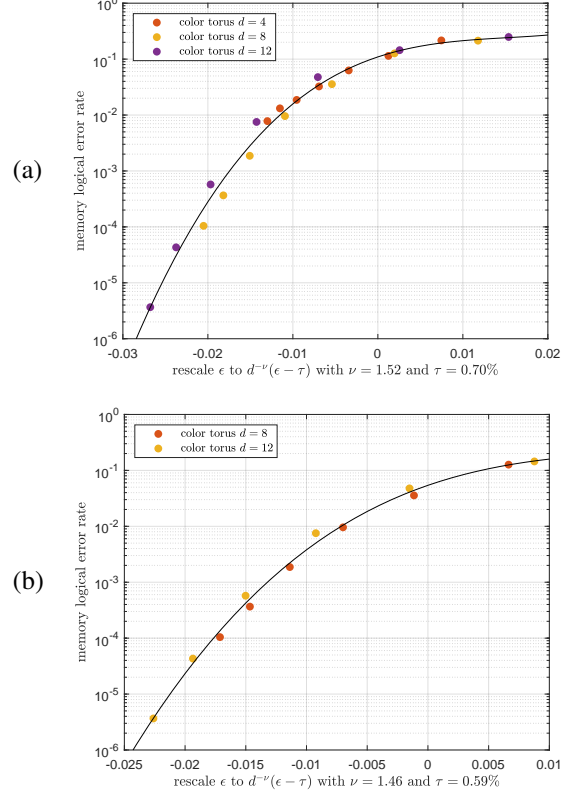


Fig. 21. Rescaled FTBP(α^*) decoding threshold performance for rotated 6.6.6 toric color codes with (a) $d = 4, 8, 12$ and (b) $d = 8, 12$.

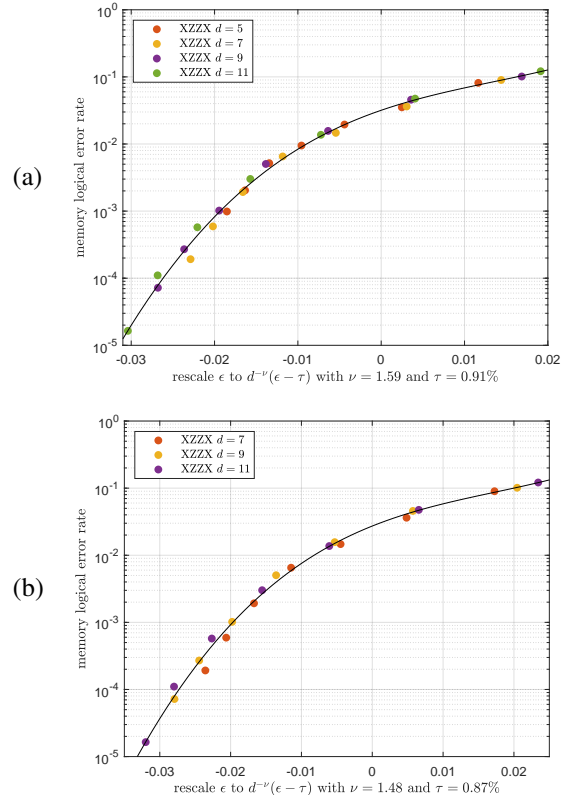


Fig. 22. Rescaled FTBP₁₆(α^*) decoding threshold performance for twisted XZZX toric codes with (a) $d = 5$ to 11 and (b) $d = 7$ to 11.